Article

A comparison of stellar populations in galaxy spheroids across a wide range of Hubble types

Proctor, RN and Sansom, Anne E

Proctor, RN and Sansom, Anne E ORCID: 0000-0002-2782-7388 (2002) A comparison of stellar populations in galaxy spheroids across a wide range of Hubble types. Monthly Notices of the Royal Astronomical Society, 333 (3). pp. 517-543. ISSN 0035-8711

Mon. Not. R. Astron. Soc. **333,** 517–543 (2002)

A comparison of stellar populations in galaxy spheroids across a wide range of Hubble types

R. N. Proctor★ and A. E. Sansom★
Centre for Astrophysics, University of Central Lancashire, Preston PR1 2HE

Accepted 2002 February 5. Received 2002 February 5; in original form 2001 July 16

ABSTRACT

We present line-strengths and kinematics from the central regions of 32 galaxies with Hubble types ranging from E to Sbc. Spectral indices, based on the Lick system, are measured in the optical and near-infrared (NIR). The 24 indices measured, in conjunction with models of the effects of varying abundance ratios, permit the breaking of age/metallicity degeneracy, and allow estimation of enhancements in specific light elements (particularly C and Mg). The large range of Hubble types observed allows direct comparison of line-strengths in the centres of early-type galaxies (E and S0) with those in spiral bulges, free from systematic differences that have plagued comparisons of results from different studies. Our sample includes field and Virgo cluster galaxies. For early-type galaxies our data are consistent with previously reported trends of Mg_2 and Mgb with velocity dispersion. In spiral bulges we find trends in all indices with velocity dispersion. We estimate luminosity-weighted ages, metallicities and heavy-element abundance ratios (enhancements) from optical indices. These show that bulges are less enhanced in light (α-capture) elements and have lower average age than early-type galaxies. Trends involving age and metallicity also differ sharply between early and late types. An anticorrelation exists between age and metallicity in early types, while, in bulges, metallicity is correlated with velocity dispersion. We consider the implications of these findings for models of the formation of these galaxies. We find that primordial collapse models of galaxy formation are ruled out by our observations, while several predictions of hierarchical clustering (merger) models are confirmed.

Key words: galaxies: abundances – galaxies: evolution – galaxies: formation – galaxies: stellar content.

1 INTRODUCTION

The bulges of spirals, and the spheroidal components of elliptical (E) and S0 galaxies, exhibit many similarities. These include their colours and colour gradients (Balcells & Peletier 1994), as well as their morphological and kinematic properties (Bender, Burstein & Faber 1993). The question then arises: do these similarities imply similar formation processes? Attempts to answer this question using morphology and kinematics have so far failed, because the observed properties are successfully reproduced by both models proposed for galaxy formation (i.e., primordial collapse, e.g. Carlberg 1984, and hierarchical collapse, e.g. Kauffmann, White & Guiderdoni 1993 and Barnes & Hernquist 1996). On the other hand, the use of photometry to constrain the models is severely hampered by the degeneracy in colours with respect to age and metallicity (Worthey 1994, hereafter W94). Thus, in galaxy populations the above properties place only weak constraints on formation mechanisms and star formation histories (SFHs).

In order to provide a more sensitive tool for probing composite populations, W94 used the Lick/IDS spectral features (Faber et al. 1985), to estimate pseudo-line-strengths (indices), for a range of single-age, single-metallicity stellar populations (SSPs). W94 demonstrated that although individual indices are affected by age/metallicity degeneracy, their sensitivities to both age and metallicity vary. Consequently, W94 was able to find combinations of indices that broke the degeneracy. Over the last few years, models of SSPs have been refined and new indices added. Vazdekis et al. (1996, hereafter V96) and Vazdekis (1999a,b, hereafter V99) used more recent (and complete) isochrones for the SSP calculations, as well as including the Mg I and Ca triplet indices in the NIR (Diaz, Terlevich & Terlevich 1989). Higher order Balmer absorption lines (Hδ and Hγ) were also included. We shall refer to the collection of the above indices as the Lick indices.

Many studies of early-type galaxies have measured small

★E-mail: rproctor@uclan.ac.uk (RNP); aesansom@uclan.ac.uk (AES)

numbers of Lick indices (Worthey, Faber & González 1992; Davies, Sadler & Peletier 1993; Gorgas et al. 1997; Greggio 1997; Trager et al. 2000a, hereafter T00a). These studies show that when the commonly observed Mg_2 or Mgb indices are plotted against indices centred on Fe features (e.g., Fe5227, Fe5335 or their average $\langle$Fe$\rangle$), most early-type galaxies lie outside the range of values covered by SSPs based on solar metal abundance ratios. In these galaxies the Mg_2 and Mgb index values are significantly larger than those of SSPs with similar Fe index values. This illustrates the well-known Mg excess in early-type galaxies (e.g. Faber 1973; O'Connell 1976; Worthey et al. 1992; Henry & Worthey 1999). Indices centred on carbon features are also seen to lie outside the range covered by SSPs (Worthey 1998; Henry & Worthey 1999), implying that C is another element whose relative abundance is enhanced in these populations. These studies also show that a positive correlation exists between central velocity dispersion and certain Mg indices (e.g. Bender et al. 1993, 1998; Kuntschner 2000, hereafter K00). These trends have been likened to trends in colour–magnitude diagrams and interpreted as a metallicity–mass relation (i.e., high metallicities are found in high velocity dispersion galaxies due to the ability of deep potential wells to retain metals; e.g. Faber 1973; Kodama et al. 1998). However, this interpretation makes no allowance for either the age/metallicity degeneracy in these indices or their enhancements with respect to other indices. It is also important to note that other metallicity-sensitive indices show weak or no trends with velocity dispersion (Fisher, Franx & Illingworth 1996; Trager et al. 1998; Jørgensen 1999).

Few studies have included spiral bulges. However, Idiart, de Freitas Pacheco & Costa (1996) and Jablonka, Martin & Arimoto (1996) observed Lick indices in the centres of bulges. They found correlations of the small number of indices observed with both bulge luminosity and velocity dispersion. Goudfrooij, Gorgas & Jablonka (1999) also report measurements of a small number of indices in bulges, and suggest that the Mg and C excess observed in early types is also present in bulges. However, in a previous study (Proctor, Sansom & Reid 2000) we found that a sample of four spiral bulges lay closer to the solar abundance ratio SSPs, in the Mg_2–$\langle$Fe$\rangle$ plane, than do early types. Unfortunately, none of the above bulge studies were emission-corrected, and only the Goudfrooij et al. study was fully calibrated to the Lick system, making full comparisons with early-type galaxies difficult. This highlights one of the advantages of the present study in which such systematic uncertainties are significantly reduced by the identical instrumentation and reduction procedures used.

While the sensitivities of Lick indices to abundances of individual elements, such as Mg and C, complicate their interpretation, they also provide a powerful tool for probing star formation histories in galaxies, using models of galactic chemical evolution (e.g. Vazdekis et al. 1997; Sansom & Proctor 1998). This is due to the difference between production sites of light elements and those of Fe− peak elements, i.e., while Mg is mainly produced in type II supernovae (SNII), Fe− peak elements are predominantly produced in type Ia supernovae (SNIa). Thus, if reasonable estimates can be made of Mg and Fe abundances, constraints can be placed on possible SFHs. To quantify the effects of individual element abundance enhancements on Lick indices, Tripicco & Bell (1995, hereafter TB95) modelled the effects of doubling 10 key elements in the synthetic spectra of three stellar types. They showed that Lick indices centred on C and Mg features (e.g., CN_1, CN_2, or their average $\langle$CN$\rangle$, $C_2$4668, Mg_1, Mg_2 and Mgb) are much more sensitive to the abundances of C and Mg than they are to overall metallicity [Z/H].[1] These indices are then more sensitive to the *abundance ratios* of C and Mg (i.e., [C/Fe] and [Mg/Fe]) than to [Z/H]. On the other hand, the sensitivities to individual elements of the Fe indices (Fe4383, Fe4531, Fe5015, Fe5270, Fe5335 and Fe5406) and Ca indices (Ca4227 and Ca4455) are comparable to, or less than, their sensitivity to [Z/H]. It is this range of sensitivities to individual elements and [Z/H] that permits estimation of ages, metallicities and abundance ratios from index values, and thus the constraining of possible SFHs, in galaxy populations.

In this paper we describe the measurement and analysis of 24 Lick indices in the centres of 32 galaxies with Hubble types ranging from E to Sbc. These galaxies were observed in a single observing run, with identical instrumental set-ups. We compare the indices and their correlations with velocity dispersion in early- and late-type galaxies. We use V99 SSPs and the data of TB95 to estimate luminosity-weighted ages, metallicities and abundance ratios in our galaxy sample. Finally, the overall trends in our data are compared to the predictions of our galactic chemical evolution code for models of galaxy formation.

In Section 2 the observations and data reductions are described, including calibrations and emission corrections. In Section 3 central values of indices and kinematics are presented. Comparison of the trends in our data are made with previous observations. Estimates of luminosity-weighted age, metallicity and abundance ratio are described in Section 4. In Section 5 we discuss the interpretation of our results in terms of composite models of possible star formation histories. In Section 6 we give some discussion of our results and draw our conclusions. Appendix A gives details of velocity dispersion corrections. In future papers and in Proctor (PhD thesis, in preparation) the spatially resolved results will be reported and the data further exploited to recover more detail of the SFHs, using galactic chemical evolution models.

2 OBSERVATIONS AND DATA REDUCTIONS

2.1 Sample selection

The data presented here are from observations made during time awarded for two separate PPARC PATT proposals. The first was to test the prediction that young elliptical galaxies should be devoid of hot gas (e.g. Ciotti et al. 1991). Bright ($B_T^0 < 13$) early-type galaxies ($-5 \leq T \leq -2$), with X-ray emission temperatures and luminosities well constrained by *ROSAT* observations, were selected. The second proposal detailed an investigation of the stellar populations along the minor axes of bright ($B_T^0 < 13$) spiral bulges ($0 \leq T \leq 4$). Highly inclined galaxies (inclination $>75°$) were selected to minimize the effects of disc contamination in the outer regions of the bulges. Highly inclined galaxies with prominent dust lanes covering the centre of the bulge were removed from the sample, as these would give little information about the bulge centres. Both studies aimed to use the same range of Lick indices to investigate the SFH of galaxies and to make estimates of luminosity-weighted ages, metallicities and abundance ratios at a number of points across the galaxies, to estimate gradients. Fortunately, the two observation runs were scheduled

[1] We use the standard notation, $[X/Y] = \log(X/Y) - \log(X_\odot/Y_\odot)$, where X and Y are the masses of either individual, or groups of, elements. The term **abundance** is used to refer to the mass of a specific element divided by that of H [X/H], while **abundance ratios** are specified with respect to Fe [X/Fe]. Overall metallicity is represented by [Z/H].

back-to-back, allowing observations to be made with identical instrument set-ups. The two studies result in a sample of 32 galaxies with 24 indices measured (Table 1).

2.2 Observations

Long-slit spectroscopic observations along the minor axes of 11 Es, six S0s and 16 spiral bulges (bulges) were obtained between 1998 February 28 and 1998 March 3 with the WHT on La Palma. The double-beam spectroscope (ISIS) was used with a 5700-Å dichroic and Tektronix 1024×1024 CCDs. On the blue arm a 300 line mm^{-1} grating was used, giving a wavelength coverage of 3995–5495 Å at a dispersion of 1.5 Å per pixel. This range covers 16 indices calibrated by Gorgas et al. (1993) and Worthey et al. (1994), including the extensively observed Mg_2 and $\langle Fe \rangle$ indices, as well as the recently calibrated Hδ and Hγ indices (Worthey & Ottaviani 1997). On the red arm a 600 line mm^{-1} grating was used, giving a wavelength coverage of 8275 to 9075 Å at a dispersion of 0.8 Å per pixel. This range covers the Mg I feature at 8807 Å and the highly metallicity-sensitive Ca II triplet (Diaz et al. 1989; V96). The plate-scale was 0.36 arcsec per pixel on both red and blue arms. The slit, of length 4 arcmin and width 1.25 arcsec, was placed along the minor axes of the galaxies, with the exception of NGC 2831 and 2832 which, being in close proximity on the sky, were observed simultaneously, i.e., with a position angle of 45° in both galaxies. A maximum exposure time of 1500 s was adopted to facilitate cosmic ray removal. Multiple exposures of individual galaxies were obtained to achieve the desired signal-to-noise ratio (giving index errors of approximately 5 per cent at $r_e/2$). Seeing was ~ 1.5 arcsec. The total exposure time and position angle of the slit are given in Table 1. Tungsten lamp exposures, for flat-fielding, were obtained each night on the blue arm. However, due to known fringing effects on the red arm, red tungsten lamp exposures were taken just before or after every object exposure, with the telescope tracking the object. A total of five flux-calibration standards and 24 stars (from Faber et al. 1985) for calibration of the Lick indices were observed. A neutral density filter (ND1.8) was used in the stellar observations. Observations of faint calibration stars and tungsten lamp exposures were obtained, with and without the neutral density filter, to allow removal of the spatial and spectral responses of the filter. The sample of Lick calibration stars was selected to possess index values spanning the range of values expected in our galaxy sample. The calibration star sample was also chosen for good overlap with stars with Hδ and Hγ measurements reported by Worthey & Ottaviani (1997), as well as stars used in the calibration of the Ca II index (Diaz et al. 1989). All calibration stars possess known heliocentric radial velocities.

Table 1. WHT Observations. *T* type, Hubble type and half-light radius (r_e) are from de Vaucouleurs et al. (1991, hereafter RC3). Central velocity dispersion (σ_0) and radial velocity (RV) are the values derived from our blue spectra, and are for the central 3.6×1.25 arcsec^2. Estimated errors are given in brackets (see Section 2.5.1 for details of derived kinematics). Distances are mainly from Tully (1988), with the exception of more distant galaxies where radial velocities from RC3 were used. Exposure times and ISIS slit position angle (PA), which is normally along the minor axis of each galaxy, are given. Group membership is from Tully (1988).

Galaxy	*T* Type	Hubble Type	r_e (″)	σ_0 (km s^{-1})	RV (km s^{-1})	Distance (Mpc)	Exposure (sec)	PA (deg)	Group
NGC2549	−2	S0	17	143(2)	1076(2)	18.8	3600	87	Ursa Major cloud
NGC2683	3	Sb	56	129(2)	427(2)	5.7	4800	134	Leo spur
NGC2832	−4	E	25	288(5)	6899(6)	91†	3600	45*	
NGC2831	−5	E		202(4)	5160(3)	68†	3600	45*	
NGC3226	−5	E	34	203(4)	1313(3)	23.4	3600	105	Leo cloud
NGC3254	4	Sbc	41	119(2)	1373(2)	23.6	5400	136	Leo cloud
NGC3301	0	S0a	20	114(2)	1338(2)	23.3	2400	142	Leo cloud
NGC3607	−2	S0	43	240(2)	930(3)	19.9	2700	30	Leo cloud
NGC3608	−5	E	34	208(3)	1219(3)	23.4	2700	165	Leo cloud
NGC3623	1	Sa	85	164(2)	801(2)	7.3	2400	84	Leo spur
NGC3769	3	Sb		46(9)	708(3)	17.0	2400	62	Ursa Major cloud
NGC4157	3	Sb	35	92(2)	780(2)	17.0	3600	156	Ursa Major cloud
NGC4192	2	Sab	95	131(2)	−105(2)	16.8	2700	65	Virgo cluster
NGC4203	−2	S0	20	193(3)	1078(2)	9.7	1200	100	Coma-Sculptor cloud
NGC4216	3	Sb	35	207(2)	131(2)	16.8	2400	109	Virgo cluster
NGC4217	3	Sb	55	95(4)	989(3)	17.0	1200	140	Ursa Major cloud
NGC4291	−5	E	17	292(4)	1701(4)	29.4	2400	20	CVC cloud
NGC4312	1.5	Sab	41	77(5)	152(3)	16.8	1200	80	Virgo cluster
NGC4313	2	Sab		69(2)	1436(2)	16.8	4800	53	Virgo cluster
NGC4365	−5	E	50	254(3)	1221(3)	16.8	2700	130	Virgo cluster
NGC4374	−5	E	51	316(5)	1019(5)	16.8	2400	45	Virgo cluster
NGC4419	1	Sa	24	101(3)	−206(2)	16.8	3600	43	Virgo cluster
NGC4526	−2	S0	44	214(3)	591(3)	16.8	1500	23	Virgo cluster
NGC4552	−4	E	29	272(4)	323(4)	16.8	1200	0	Virgo cluster
NGC4636	−5	E	89	243(3)	919(3)	17.0	2400	60	Virgo cluster
NGC4697	−5	E	67	194(2)	194(2)	23.3	1200	160	Virgo cluster
NGC5322	−5	E	34	233(3)	1801(3)	31.6	2400	5	CVC cloud
NGC5354	−2	S0	18	221(3)	2580(3)	33†	1200	0	
NGC5353	−2	S0	15	280(4)	2230(4)	37.8	1200	0	CVC cloud
NGC5746	3	Sb	75	192(2)	1704(2)	24†	3600	80	Virgo-Libra cloud
NGC5908	3	Sb	29	152(2)	3340(2)	29.4	4800	64	
NGC5987	3	Sb	30	177(2)	3005(2)	40†	2400	165	

* Not along minor axis (Section 2.2).
† Distances calculated from radial velocities given in RC3 assuming $H_0 = 75$ km s^{-1} Mpc^{-1}.

2.3 Basic reductions

Unless otherwise stated, data reductions were carried out using the CCDPACK, FIGARO and KAPPA packages of Starlink software. Bias removal was carried out by the subtraction of an average bias frame, normalized to the average value in the over-scan region, in each object frame. After conversion from electrons to photons, variance arrays were generated and propagated throughout the reductions. In the blue, flat-fielding was achieved by division of target frames by the normalized average of tungsten lamp exposures obtained on the same night. However, on the last night suitable tungsten lamp exposures were not obtained. For this night the flat-field from the first day was used (the day for which arc exposures were most similar). Division of target frames by tungsten lamp exposures leaves the spectra biased by the smooth spectral response of the lamp. This is removed at flux calibration. However, during the flat-fielding procedure, features in the blue tungsten lamp spectra were identified that moved independently of wavelength calibration. The features were in the range 4000–4600 Å, and were identified with features in the dichroic response. The effects of these features are included in our statistical errors, as detailed in Section 2.4.2. Flat-fielding of the red data was carried out by division of each target frame by the normalized average of the bracketing tungsten lamp exposures. Stellar frames were divided by the normalized neutral density filter response. Cosmic rays and bad rows were removed by interpolation across the affected areas. Wavelength calibration was carried out by comparison with arc lamp exposures taken just before and/or after each exposure. An accuracy of better than 0.1 Å was consistently achieved in both red and blue calibrations. All object frames were extinction-corrected using the extinction curve appropriate for La Palma. Flux calibrations derived from multiple observations of single stars varied by less than 1.5 per cent across the region of CCD used, while those derived from different stars varied by less than ~5 per cent. All frames were flux-calibrated using the average of the calibration curves of five flux-calibration stars. Sky estimates were made using the outermost regions of the slit that were not significantly vignetted. After sky subtraction, galaxy frames were co-added to form a single frame for each galaxy. The spiral galaxy NGC 4100 was found to be dominated by emission, and was excluded from further analysis. Due to the presence of telluric absorption lines above 8920 Å, reliable near-infrared (NIR) indices could not be determined for galaxies with recession velocities above 2200 km s^{-1} (i.e., NGC 2831, 2832, 5353, 5354, 5908 and 5987).

2.4 Calibrations using stellar spectra

The original calibrations of stellar line-strengths with photospheric parameters, upon which the SSPs used here are based, were carried out using data from the Lick/IDS scanner (Faber et al. 1985). This instrument has a spectral resolution that varies with wavelength (Worthey & Ottaviani 1997). The Lick data were also not flux-calibrated. Therefore, in order to calibrate our index measurements to the Lick system, it is necessary to compensate for both the differences in flux calibration between our data and that in the calibration data, as well as the differences in spectral resolution achieved.

2.4.1 Correction for spectral resolution

For each index, the value of the Lick spectral resolution (σ_L in Table 2) was estimated from fig. 7 of Worthey & Ottaviani (1997), at the wavelength of the mid-point of the central band. The spectra of our sample of Lick calibration stars were then broadened to the appropriate calibration resolution (σ_L), for each index, by convolution with a Gaussian of width σ_B given by

$$\sigma_B^2 = \sigma_L^2 - \sigma_I^2. \quad (1)$$

The instrumental broadening for our data (σ_I) was estimated from arc lines, and found to be 1.5 Å in the blue and 0.7 Å in the NIR. After appropriate broadening, stellar indices were evaluated using our own code. Wavelength-range definitions supplied by Worthey on his home page were used. For the NIR indices, band definitions and calibration resolution (σ_L) were taken from Diaz et al. (1989) (after allowing for a typographical error). Our code was tested using the stellar data also provided on Worthey's home page for this purpose. Differences between the values given by Worthey and those derived by our code from the provided spectra were $\leq$0.03 Å for the line features, and $\leq$0.002 mag for molecular band indices. These discrepancies are smaller than differences caused by recalibration of Worthey's data to our wavelength resolution, and are probably the result of differences in the handling of partial bins.

2.4.2 Flux-calibration correction

In order to compensate for the differences in flux calibration between our data and the stellar calibration spectra, the difference between measured and published values was calculated, for each index, in each of the observed calibration stars. For all indices except G4300, we found no significant correlation between these differences and the measured values. Therefore, for all indices except G4300, the average difference is used as a final correction to the velocity dispersion corrected values. For G4300, the differences between measured ($G4300_{raw}$) and published values exhibited a correlation with $G4300_{raw}$ given by

$$Offset = 4.340 - 0.749 \times G4300_{raw}. \quad (2)$$

The final correction to the velocity dispersion corrected values of G4300 was therefore calculated using this equation. However, for one galaxy (NGC 3769), $G4300_{raw}$ lay significantly outside the range of values covered by our stellar sample. Consequently, the value of G4300 for this galaxy, while reported here, was omitted from further analysis. Comparison of the measured indices in the calibration sample with the published data is shown in Table 2. For blue indices with band definitions above 4600 Å, the rms scatter about the offset in our sample is generally dominated by the rms error associated with individual Lick observations. However, the scatter in our data is significantly greater than this error for indices with band definitions below 4600 Å (with the exception of Ca4227). This is the wavelength range affected by the poor removal of the dichroic response identified in Section 2.3. For indices in this wavelength range the excess scatter (calculated in quadrature) of our data compared to the Lick error has been included in our error calculations. This turns out to be a conservative error estimate for all indices but Ca4227, whose error we assume to be underestimated. For the NIR indices, differences between the stellar data of Diaz et al. (1989) and our stellar data were used for flux-calibration correction. We note that the scatter in our data is greater than the rms error per single observation in the Diaz et al. data (given as typically 5 per cent). However, these indices are not used for the purposes of absolute age/metallicity estimates, and this uncertainty has not been included in our errors.

Table 2. The resolution of the Lick calibrations (σ_L) are given for reported indices. For all indices, with the exception of G4300, offsets represent average differences between the published index values and our observations for 24 Lick calibration stars. For G4300 the offset was modelled as a function of the observed value (see text). N.B. ⟨Fe⟩ is the average of Fe5270 and Fe5335, while CaT is the sum of Ca2 and Ca3.

Index	Unit	σ_L (Å)	Lick Offset	rms scatter about offset	rms error per Lick observation
$H\delta_A$	Å	4.64	0.209	0.819*	0.64
$H\delta_F$	Å	4.64	−0.048	0.410*	0.40
CN_1	mag	4.51	−0.018	0.038*	0.021
CN_2	mag	4.51	−0.009	0.037*	0.023
Ca4227	Å	4.34	0.027	0.189*	0.27
G4300	Å	4.17	†	0.656*	0.39
$H\gamma_A$	Å	4.04	0.561	1.014*	0.48
$H\gamma_F$	Å	4.04	0.258	0.891*	0.33
Fe4383	Å	3.91	1.137	1.739*	0.53
Ca4455	Å	3.87	0.226	0.454*	0.25
Fe4531	Å	3.83	0.370	0.697*	0.42
$C_2$4668	Å	3.74	−0.276	0.437	0.64
$H\beta$	Å	3.61	−0.093	0.141	0.22
Fe5015	Å	3.57	0.211	0.423	0.46
Mg_1	mag	3.57	0.007	0.006	0.007
Mg_2	mag	3.57	0.029	0.007	0.008
Mgb	Å	3.57	0.126	0.173	0.23
Fe5270	Å	3.57	0.032	0.173	0.28
Fe5335	Å	3.57	−0.040	0.238	0.26
⟨Fe⟩	Å	3.57	−0.004	0.147	0.19
Fe5406	Å	3.57	0.053	0.129	0.20
Ca1	Å	3.50	0.190	0.195	0.1**
Ca2	Å	3.50	0.208	0.226	0.2**
Ca3	Å	3.50	−0.088	0.333	0.2**
CaT	Å	3.50	0.120	0.402	0.28
Mg I	Å	3.50	0.031	0.093	0.04**

* Features affected by dichroic response.
** Typical error given by Diaz et al. (1989) as 5 per cent.
† Lick offset = $4.34 - 0.749 \times G4300_{raw}$ (see Section 2.4.2).

For all indices, the error in calibration to the Lick system was calculated as the standard error in the stellar data, i.e., $\frac{rms}{\sqrt{N-1}}$, where $N = 24$ is the number of calibration stars.

2.5 Analysis of galaxy spectra

To derive accurate indices from a galaxy spectrum, it is first necessary to obtain accurate estimates of recession velocity and velocity dispersion from the spectra. This allows the redshift to be taken into account, and the indices to be corrected for velocity dispersion (using the polynomials detailed in Appendix A). Galaxy data must also be corrected for flux calibration (Section 2.4.2) and emission.

2.5.1 *Measurement of galaxy kinematics*

Measurements of galaxy kinematics were carried out on both the red and blue data using the Fourier quotient technique within the IRAF software package. This technique was used as the associated statistical errors are significantly less than those associated with the cross-correlation technique at the low velocity dispersions typical of spiral bulges. For the purposes of velocity dispersion analysis, $H\beta$ and [O III]5007 emission lines were removed by linear interpolation across affected regions in galaxies showing strong emission. Velocity dispersion and recession velocity were estimated using each of the calibration stars. Final values and errors were taken as the average and standard error in the individual estimates. Typical errors for velocity dispersion and recession velocity were found to be $\sim 3.1\,km\,s^{-1}$ and $\sim 2.6\,km\,s^{-1}$ respectively. A comparison of our results for velocity dispersion with the average values in Prugniel & Simien (1997) is shown in Fig. 1. In this figure the average value and rms scatter in the individual measurements quoted by Prugniel & Simien are taken as the velocity dispersion and its error respectively. Despite differences in spectral and spatial sampling, agreement is reasonably good between the data sets, with a one-to-one line having a reduced χ^2 of 1.7. Our galaxy indices were corrected for velocity dispersions, as described in Appendix A.

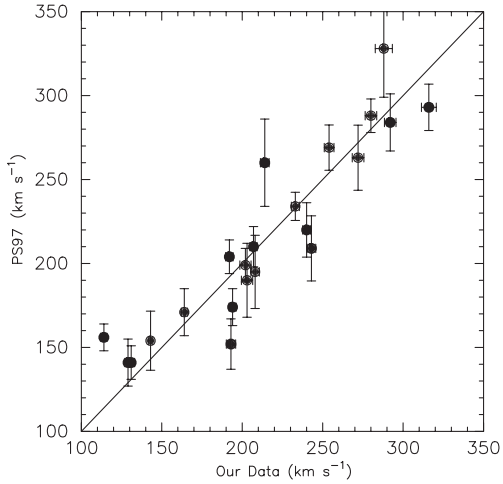

Figure 1. Comparison of measured central velocity dispersions with average values from Prugniel & Simien (1997) for 22 galaxies common to both studies. The one-to-one line is shown. Prugniel & Simien errors were estimated as the rms scatter in the individual measurements included in the data base, which employ a large range of measurement methods and apertures. Errors in our data are the standard errors in values derived from individual calibration stars for each galaxy.

2.5.2 *Emission correction*

The $H\beta$, $H\gamma$ and $H\delta$ indices suffer from line-filling in galaxies exhibiting emission. Fe5015 is also affected by [O III]5007 emission in such galaxies, while Mgb is affected by [N I]5199 emission (Goudfrooij & Emsellem 1996). We estimated [O III]5007 emission in all galaxy spectra in an effort to compensate for the effects of emission in $H\beta$, γ, δ and Fe5015. No attempt was made to estimate the (relatively small) corrections to Mgb. Following a procedure similar to that used by González (1993), each galaxy spectrum was divided by a series of template spectra. These templates were made by redshifting and broadening each star used in the blue kinematic analysis to the measured galaxy values. The aim of dividing the galaxy spectrum by a well-matching template is to remove common spectral features around the [O III] line prior to the measurement of its equivalent width. The band definitions used for our [O III] line index are as follows:

Side-band 1: 4990.0–5001.0 Å,
Centre band: 5001.0–5011.0 Å,
Side-band 2: 5011.0–5022.0 Å.

The average of values derived using each stellar template was taken as the [O III] index for each galaxy. The use of the average of a group of well-matching stellar spectra differs from the method used by González (1993) of creating individual templates for each

Table 3. Central index values (first line) and errors (second line) for the WHT sample of galaxies.

Galaxy NGC	$H\delta_A$ (Å)	$H\delta_F$ (Å)	CN_1 (mag)	CN_2 (mag)	Ca4227 (Å)	G4300 (Å)	$H\gamma_A$ (Å)	$H\gamma_F$ (Å)	Fe4383 (Å)	Ca4455 (Å)	Fe4531 (Å)	$C_2$4668 (Å)	$H\beta$ (Å)	OIII (Å)	Fe5015 (Å)	Mg_1 (mag)	Mg_2 (mag)	Mgb (Å)	Fe5270 (Å)	Fe5335 (Å)	Fe5406 (Å)
2549	−2.129	0.079	0.080	0.123	1.330	5.474	−5.298	−1.522	7.271	1.748	3.813	8.561	2.012	−0.177	6.457	0.142	0.307	4.421	3.450	3.023	2.171
	0.553	0.144	0.033	0.031	0.055	0.554	0.930	0.858	1.711	0.396	0.584	0.132	0.072	0.077	0.148	0.002	0.003	0.055	0.058	0.074	0.048
2683	−0.699	0.735	−0.011	0.023	1.243	5.382	−3.317	0.337	7.147	1.128	3.690	5.131	2.192	−1.528	5.597	0.112	0.255	3.971	2.879	2.278	1.650
	0.563	0.161	0.034	0.032	0.075	0.561	0.936	0.861	1.715	0.402	0.591	0.185	0.096	0.089	0.192	0.003	0.004	0.077	0.083	0.102	0.071
2832	−2.788	0.056	0.164	0.219	1.389	6.036	−7.238	−1.700	7.215	1.596	3.890	8.531	1.471	−0.064	5.514	0.157	0.354	5.278	3.036	2.892	
	0.561	0.156	0.034	0.031	0.072	0.558	0.933	0.859	1.715	0.402	0.590	0.178	0.076	0.039	0.186	0.003	0.004	0.082	0.088	0.108	
2831	−1.161	0.465	0.065	0.107	0.832	5.395	−3.026	−0.363	4.353	1.500	3.716	6.950	1.609	−0.478	5.605	0.114	0.286	4.348	2.625	2.691	
	0.571	0.173	0.034	0.032	0.090	0.567	0.939	0.861	1.719	0.405	0.596	0.225	0.104	0.067	0.222	0.005	0.006	0.101	0.112	0.133	
3226	−1.066	0.675	0.119	0.158	1.376	5.469	−5.123	−1.331	6.700	1.586	3.278	7.535	1.374	−2.249	4.672	0.171	0.334	5.419	2.785	2.374	1.931
	0.564	0.162	0.034	0.032	0.076	0.561	0.936	0.861	1.715	0.402	0.591	0.184	0.093	0.077	0.191	0.003	0.004	0.078	0.086	0.104	0.073
3254	−1.141	0.996	0.044	0.082	1.064	5.848	−4.466	0.650	6.297	1.155	3.750	5.179	2.777	−2.495	6.148	0.101	0.246	3.924	2.866	2.403	1.740
	0.562	0.159	0.034	0.032	0.072	0.559	0.936	0.861	1.714	0.401	0.589	0.178	0.099	0.100	0.193	0.003	0.004	0.076	0.082	0.099	0.070
3301	1.258	1.556	−0.010	0.030	1.069	5.414	−2.067	0.016	4.973	1.470	2.966	5.579	2.128	−0.537	5.478	0.085	0.206	3.380	2.768	2.287	1.708
	0.554	0.146	0.033	0.031	0.059	0.555	0.931	0.859	1.712	0.398	0.586	0.146	0.080	0.084	0.161	0.002	0.003	0.061	0.065	0.083	0.055
3607	−2.921	−0.036	0.144	0.186	1.172	6.102	−6.732	−1.260	6.049	1.766	4.034	8.358	1.580	−0.673	6.321	0.159	0.323	5.263	3.169	3.091	2.062
	0.555	0.147	0.033	0.031	0.061	0.555	0.931	0.858	1.712	0.398	0.585	0.145	0.068	0.056	0.154	0.003	0.003	0.062	0.066	0.082	0.057
3608	−2.316	−0.140	0.105	0.155	1.330	5.370	−5.371	−1.975	7.340	1.734	3.583	7.898	1.515	−0.193	5.933	0.168	0.338	5.048	3.072	2.612	2.025
	0.556	0.148	0.033	0.031	0.062	0.556	0.931	0.858	1.712	0.398	0.586	0.148	0.073	0.064	0.157	0.003	0.003	0.064	0.069	0.084	0.058
3623	−2.796	0.056	0.093	0.133	1.340	5.770	−6.047	−1.208	6.867	1.596	3.970	7.552	1.664	−0.642	6.278	0.141	0.309	4.803	3.360	3.102	2.169
	0.558	0.152	0.034	0.031	0.064	0.556	0.933	0.859	1.712	0.399	0.587	0.156	0.080	0.077	0.165	0.003	0.003	0.065	0.069	0.086	0.058
3769	5.392	3.914	−0.115	−0.072	0.367	4.565	3.753	3.539	2.233	0.810	1.972	1.507	2.435	−1.005	3.394	0.033	0.105	1.672	1.618	1.480	0.775
	0.573	0.180	0.035	0.033	0.107	0.582	0.945	0.865	1.730	0.418	0.616	0.330	0.152	0.096	0.325	0.007	0.009	0.153	0.173	0.207	0.157
4157	0.364	1.191	−0.006	0.030	0.694	5.871	−4.449	−0.331	4.143	1.269	3.478	4.096	1.049	−0.410	4.652	0.081	0.203	3.161	2.542	2.147	1.448
	0.617	0.235	0.038	0.037	0.146	0.599	0.969	0.873	1.741	0.430	0.627	0.360	0.161	0.086	0.328	0.007	0.009	0.150	0.163	0.193	0.143
4192	0.095	1.286	0.045	0.081	1.130	5.605	−3.529	−0.192	4.550	1.830	2.956	6.859	2.088	−0.963	6.040	0.116	0.241	4.012	2.925	2.802	1.756
	0.564	0.162	0.034	0.032	0.076	0.560	0.936	0.861	1.715	0.401	0.591	0.182	0.092	0.085	0.185	0.003	0.004	0.074	0.080	0.096	0.068
4203	−3.054	0.337	0.192	0.234	1.102	6.146	−7.019	−0.458	6.812	1.614	4.404	8.490	1.564	−2.282	5.712	0.175	0.338	5.354	3.266	3.152	2.102
	0.562	0.158	0.034	0.032	0.072	0.558	0.936	0.860	1.714	0.401	0.589	0.175	0.091	0.081	0.186	0.003	0.004	0.075	0.082	0.100	0.071
4216	−3.022	−0.041	0.114	0.157	1.371	5.662	−6.003	−1.285	7.701	1.606	4.092	9.041	1.897	−0.584	6.354	0.173	0.339	4.953	3.566	3.187	2.128
	0.559	0.153	0.034	0.031	0.066	0.557	0.933	0.859	1.712	0.399	0.587	0.154	0.075	0.067	0.159	0.003	0.003	0.064	0.068	0.084	0.057
4217	−0.236	1.579	0.011	0.052	0.449	5.524	−2.664	0.666	4.761	1.084	3.165	3.166	1.330	−0.572	5.123	0.064	0.184	3.008	3.045	2.343	1.526
	1.139	0.673	0.072	0.081	0.491	1.018	1.324	1.028	2.052	0.718	0.991	1.186	0.501	0.088	1.015	0.025	0.030	0.500	0.537	0.628	0.486
4291	−3.449	−0.203	0.134	0.186	1.099	5.740	−6.943	−0.806	7.546	1.353	4.514	6.784	1.435	−0.043	6.012	0.146	0.318	5.268	3.082	2.578	1.940
	0.555	0.146	0.033	0.031	0.061	0.555	0.931	0.858	1.714	0.400	0.588	0.152	0.064	0.039	0.166	0.003	0.004	0.068	0.070	0.087	0.066
4312	2.841	2.192	−0.053	−0.027	0.765	5.767	−1.881	−0.071	0.597	1.289	1.885	3.171	0.063	−0.502	3.830	0.049	0.130	2.386	1.828	2.222	1.301
	0.836	0.464	0.053	0.058	0.328	0.774	1.127	0.947	1.923	0.572	0.846	0.882	0.394	0.087	0.792	0.019	0.023	0.381	0.428	0.493	0.379
4313	0.444	1.530	0.005	0.047	0.795	5.533	−2.962	1.453	6.046	1.155	3.825	5.530	2.732	−0.934	6.204	0.082	0.217	3.239	2.851	2.443	1.549
	0.568	0.168	0.034	0.032	0.084	0.565	0.939	0.862	1.717	0.405	0.594	0.210	0.106	0.094	0.211	0.004	0.005	0.089	0.097	0.115	0.084
4365	−2.164	−0.087	0.095	0.143	1.574	5.272	−5.442	−1.832	7.890	1.622	3.788	8.081	1.617	0.017	6.396	0.169	0.355	5.354	3.335	2.808	2.130
	0.556	0.148	0.034	0.031	0.062	0.556	0.931	0.858	1.712	0.398	0.586	0.152	0.068	0.048	0.160	0.003	0.003	0.067	0.070	0.088	0.063
4374	−2.199	−0.102	0.088	0.132	1.432	5.348	−5.217	−1.480	8.201	1.422	3.837	7.299	1.225	−0.595	5.638	0.167	0.335	5.414	2.989	2.739	2.010
	0.555	0.146	0.033	0.031	0.063	0.555	0.931	0.858	1.717	0.403	0.589	0.154	0.064	0.036	0.172	0.003	0.004	0.071	0.070	0.089	0.070
4419	1.877	2.038	−0.055	−0.024	0.697	5.067	−0.128	2.215	6.198	1.015	3.919	4.993	2.183	−1.433	5.171	0.089	0.203	3.174	2.463	2.143	1.435
	0.561	0.159	0.034	0.032	0.076	0.561	0.935	0.860	1.715	0.402	0.591	0.188	0.099	0.093	0.196	0.003	0.004	0.079	0.085	0.104	0.073
4526	−1.424	0.458	0.051	0.095	1.128	5.058	−3.643	−0.090	8.669	1.228	4.384	7.940	1.588	−0.170	6.103	0.154	0.317	4.579	3.518	3.014	2.150
	0.559	0.154	0.034	0.031	0.069	0.559	0.933	0.859	1.713	0.400	0.589	0.172	0.080	0.061	0.173	0.003	0.004	0.074	0.078	0.098	0.069
4552	−2.364	−0.082	0.105	0.152	1.165	5.260	−4.688	−0.325	9.350	1.096	4.785	8.660	1.330	−0.154	5.825	0.192	0.367	5.392	3.237	2.890	2.048
	0.557	0.150	0.034	0.031	0.065	0.557	0.931	0.858	1.713	0.399	0.588	0.159	0.070	0.044	0.167	0.003	0.004	0.070	0.074	0.091	0.067
4636	−3.346	−0.151	0.157	0.203	1.223	6.267	−7.257	−1.407	5.510	1.739	4.280	8.239	1.452	−0.603	5.871	0.166	0.339	5.340	3.189	2.905	2.081
	0.562	0.157	0.034	0.032	0.072	0.558	0.934	0.859	1.714	0.400	0.589	0.174	0.081	0.055	0.181	0.003	0.004	0.079	0.085	0.103	0.075

Table 3 – *continued*

Galaxy NGC	$H\delta_A$ (Å)	$H\delta_F$ (Å)	CN_1 (mag)	CN_2 (mag)	Ca4227 (Å)	G4300 (Å)	$H\gamma_A$ (Å)	$H\gamma_F$ (Å)	Fe4383 (Å)	Ca4455 (Å)	Fe4531 (Å)	C_24668 (Å)	$H\beta$ (Å)	OIII (Å)	Fe5015 (Å)	Mg_1 (mag)	Mg_2 (mag)	Mgb (Å)	Fe5270 (Å)	Fe5335 (Å)	Fe5406 (Å)
4697	−3.670	−0.237	0.141	0.187	1.247	6.061	−7.339	−0.775	7.132	1.336	4.391	8.600	1.612	−0.045	5.933	0.151	0.320	5.082	3.447	3.006	2.040
	0.564	0.159	0.034	0.032	0.071	0.559	0.935	0.859	1.714	0.401	0.589	0.173	0.083	0.067	0.177	0.003	0.004	0.074	0.080	0.098	0.069
5322	−1.674	0.238	0.061	0.105	1.427	5.619	−4.929	−2.027	6.115	1.951	3.176	7.339	1.846	−0.150	6.176	0.129	0.298	4.554	3.287	2.849	1.953
	0.556	0.148	0.033	0.031	0.062	0.556	0.931	0.858	1.712	0.398	0.586	0.154	0.071	0.055	0.159	0.003	0.003	0.067	0.071	0.089	0.062
5354	−2.002	0.170	0.101	0.142	1.481	6.032	−4.661	−1.554	5.342	1.568	3.375	7.839	1.802	−0.858	6.185	0.153	0.325	4.952	2.990	2.880	1.922
	0.582	0.188	0.035	0.033	0.101	0.572	0.946	0.864	1.723	0.411	0.603	0.251	0.115	0.062	0.247	0.005	0.007	0.112	0.123	0.145	0.109
5353	−2.592	−0.243	0.146	0.193	1.436	5.828	−5.783	−2.639	6.001	1.884	3.859	9.260	1.339	−0.437	6.926	0.183	0.370	5.447	3.376	2.989	2.196
	0.570	0.170	0.034	0.032	0.085	0.564	0.939	0.861	1.718	0.407	0.597	0.216	0.095	0.043	0.223	0.004	0.006	0.099	0.106	0.128	0.096
5746	−2.047	0.253	0.075	0.118	1.393	5.754	−5.589	−1.436	6.507	1.535	3.859	7.408	1.740	−0.612	6.399	0.144	0.326	4.735	3.202	2.941	2.141
	0.576	0.179	0.035	0.033	0.092	0.568	0.942	0.863	1.719	0.406	0.596	0.218	0.101	0.071	0.212	0.004	0.005	0.093	0.099	0.119	0.086
5908	−0.533	0.421	0.029	0.072	1.304	5.516	−6.243	−1.475	7.489	1.327	4.124	7.202	1.994	−0.675	6.260	0.105	0.273	4.295	3.320	2.701	1.844
	0.572	0.176	0.034	0.033	0.087	0.567	0.940	0.862	1.717	0.405	0.595	0.214	0.103	0.080	0.211	0.004	0.005	0.092	0.100	0.119	0.090
5987	−1.456	0.364	0.058	0.099	1.220	5.610	−5.649	−1.147	7.023	1.666	3.842	7.564	1.790	−0.432	6.468	0.116	0.278	4.353	3.257	2.635	1.876
	0.563	0.161	0.034	0.032	0.075	0.561	0.936	0.860	1.715	0.402	0.591	0.188	0.089	0.073	0.189	0.004	0.004	0.082	0.089	0.106	0.079

galaxy. Also, [O III] band definitions differ between the two methods. González estimated [O III] emission in four galaxies common with our sample, while three of the galaxies were observed by Kuntschner et al. (2001). Differences in slit width and orientation make direct comparison difficult. However, the results are in reasonable agreement ($\sim \pm 0.15$ Å). The results of our O III estimates are given in Table 3.

Osterbrock (1989) shows that the line-strengths of Hδ and Hγ in emission are less than Hβ, with line-intensities relative to Hβ of approximately 0.25 and 0.5 respectively across a large range of conditions. However, the continuum level in the spectra of all our galaxies show a reduction of approximately 50 per cent between Hβ and Hγ. Therefore, using our estimates of [O III] emission, the Gonzalez (1993) correlation between [O III] and Hβ emission, and Osterbrock (1989) data for Hγ and Hδ, we applied the following corrections:

$$\mathrm{Fe5015} = \mathrm{Fe5015_{raw}} + \Delta\mathrm{Fe5015}, \quad \Delta\mathrm{Fe5015} = -[\mathrm{O\,III}],$$
$$\mathrm{H}\beta = \mathrm{H}\beta_{\mathrm{raw}} + \Delta\mathrm{H}\beta, \quad \Delta\mathrm{H}\beta = -0.7[\mathrm{O\,III}],$$
$$\mathrm{H}\gamma = \mathrm{H}\gamma_{\mathrm{raw}} + \Delta\mathrm{H}\gamma, \quad \Delta\mathrm{H}\gamma = -0.7[\mathrm{O\,III}],$$
$$\mathrm{H}\delta = \mathrm{H}\delta_{\mathrm{raw}} + \Delta\mathrm{H}\delta, \quad \Delta\mathrm{H}\delta = -0.35[\mathrm{O\,III}].$$

It can be seen that, due to the reduction in continuum level, Hγ is as sensitive to emission in absolute terms (Å) as Hβ, while the Hδ feature is only half as sensitive. However, due to the range of strengths of both Hδ and Hγ in SSPs, estimates of age and metallicity made using these indices are significantly less affected by emission than those made using the Hβ index.

An Hβ emission index similar to the [O III] emission index described above was also defined as a check on the [O III] index. Comparison of [O III] and Hβ *emission* indices showed that most galaxies follow the Gonzalez (1993) correlation well. However, six galaxies were noted (all spiral bulges) with significantly aberrant behaviour. Three bulges (NGC 4157, 4217 and 4312) show Hβ emission substantially greater than that expected from the [O III], while three (NGC 3254, 3769 and 4313) show strong [O III], but with no detectable Hβ emission. These late-type galaxies do not follow the González correlation. Hβ values for these six galaxies are omitted from our analysis.

3 RESULTS

3.1 Central values

Central values for velocity dispersion, given in Table 1, are those derived from the central 3.6×1.25 arcsec^2 of the blue observations with centres defined as luminosity peaks. Velocity dispersion values derived using blue spectra are greater than those derived from NIR spectra by an average of $\sim 10\,\mathrm{km\,s^{-1}}$, with a scatter about this of $\sim 20\,\mathrm{km\,s^{-1}}$. However, velocity dispersion profiles in some galaxies (e.g., NGC 4192) differ significantly between blue and NIR data. This suggests that the two wavelength ranges may be detecting differing kinematic populations.

Central index values and errors for blue indices are given in Table 3. Values for Fe5406 in NGC 2831 and 2832 were not determined due to the high recession velocity of these galaxies redshifting the blue side-band of this index outside the observed spectral range. Indices are corrected for both velocity dispersion and emission, and converted to the Lick system. Reduction and calibration errors have all been included in the quoted errors. Also included, for indices with band definitions below 4600 Å, are the errors due to poor removal of the dichroic response (Section 2.4.2). Comparison of the results of our index measurements with galaxies

in common with Trager (1998) are shown in Fig. 2. Two galaxies from the study of Davies et al. (1993) are included for the Fe indices. The velocity-dispersion-sensitive Fe5270 and Fe5335 indices agree within errors. However, for Mg_2, an offset of ~ 0.008 mag is observed. Such an offset would cause metallicity and abundance ratio estimates, made using this index alone, to vary by ~ 0.04 dex. Part of the offset is probably the result of the slightly wider (1.4 arcsec) and longer (4 arcsec) aperture used in the Lick/IDS observations reported in Trager's thesis. Increasing the size of the central region from 3.6×1.25 arcsec^2 to 4.5×1.25 arcsec^2 (equal surface area) in our measurements results in an average reduction in Mg_2 of ~ 0.002 mag, while Fe5270 and Fe5335 are both reduced by ~ 0.01 Å. We therefore conclude that, for these indices at least, our data contain no significant systematic biases compared to previous observations.

In Table 4, values and errors for the fully calibrated NIR calcium triplet and Mg I features are presented. Values are from the central 3.6×1.25 arcsec^2, based on luminosity peaks in the NIR. Quoted errors include reduction, calibration and velocity dispersion errors. The velocity dispersion correction was based on velocity dispersion values derived from the NIR galaxy spectra.

3.2 Correlations between kinematics and indices

3.2.1 Early-type galaxies

Correlations between indices sensitive to α-elements (e.g., Mg_2 and Mgb) and velocity dispersion have been widely observed in early-type galaxies (Bender et al. 1993; González 1993; Jørgensen 1997; Bernardi et al. 1998; Concannon, Rose & Caldwell 2000; Kuntschner 2000; Trager et al. 2000b). Fig. 3 summarizes results for Mg_2 and Mgb from these studies. Although there is generally

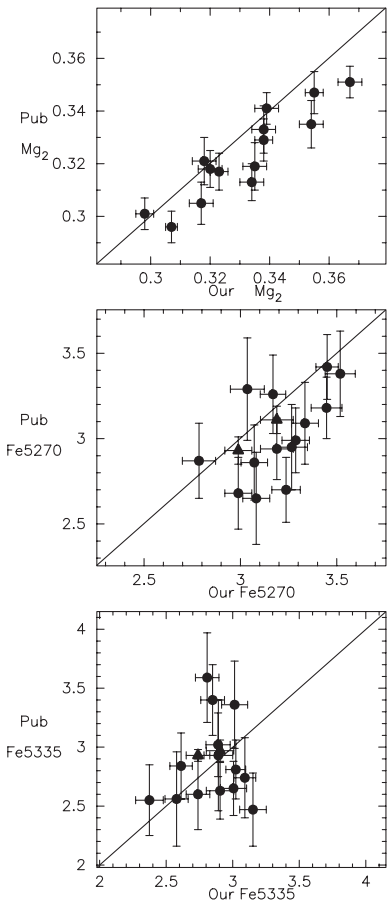

Figure 2. Comparison of our results for early-type galaxies to published data from Trager (1998) for commonly quoted indices. Also shown as triangles are results for Fe5270 and Fe5335 for two galaxies from Davies et al. (1993).

Table 4. NIR central index values (first line) and errors (second line). All reduction and calibration errors are included in the errors. Omitted galaxies are those whose high recession velocities redshift one side-band of these indices into the region of the spectrum affected by telluric lines.

Galaxy	Ca1 (Å)	Ca2 (Å)	Ca3 (Å)	Mg I (Å)
NGC 2549	1.774	4.528	3.878	0.759
	0.078	0.076	0.062	0.042
NGC 2683	1.697	4.201	3.685	0.665
	0.101	0.092	0.079	0.057
NGC 2832	–	–	–	–
NGC 2831	–	–	–	–
NGC 3226	1.737	4.242	3.483	0.910
	0.117	0.110	0.100	0.071
NGC 3254	1.687	4.175	3.650	0.671
	0.116	0.106	0.097	0.068
NGC 3301	1.623	4.355	3.775	0.575
	0.094	0.088	0.074	0.051
NGC 3607	1.639	4.169	3.552	0.806
	0.091	0.089	0.079	0.059
NGC 3608	1.797	4.263	3.634	0.854
	0.100	0.096	0.086	0.060
NGC 3623	1.711	4.181	3.658	0.748
	0.092	0.086	0.072	0.051
NGC 3769	1.745	3.965	3.561	0.550
	0.300	0.268	0.277	0.222
NGC 4157	1.573	4.073	3.730	0.543
	0.188	0.167	0.161	0.131
NGC 4192	1.966	4.458	4.170	0.652
	0.095	0.089	0.075	0.051
NGC 4203	1.797	4.276	3.573	0.864
	0.121	0.111	0.101	0.069
NGC 4216	1.794	4.159	3.743	0.732
	0.086	0.082	0.070	0.046
NGC 4217	2.427	4.827	3.877	0.770
	0.574	0.518	0.576	0.446
NGC 4291	1.652	4.197	3.429	0.679
	0.105	0.104	0.096	0.075
NGC 4312	1.530	3.535	3.989	0.344
	0.596	0.518	0.523	0.331
NGC 4313	1.734	4.622	4.145	0.710
	0.124	0.112	0.102	0.072
NGC 4365	1.900	4.430	3.699	0.723
	0.109	0.105	0.098	0.074
NGC 4374	1.740	4.109	3.438	0.597
	0.104	0.102	0.095	0.075
NGC 4419	1.854	4.143	3.813	0.630
	0.106	0.099	0.088	0.060
NGC 4526	1.910	4.311	3.793	0.823
	0.116	0.108	0.099	0.068
NGC 4552	1.603	3.771	3.257	0.705
	0.111	0.105	0.097	0.074
NGC 4636	1.629	4.009	3.539	0.707
	0.128	0.119	0.111	0.081
NGC 4697	1.660	4.343	3.625	0.703
	0.110	0.102	0.092	0.062
NGC 5322	1.858	4.471	3.635	0.778
	0.110	0.105	0.097	0.072
NGC 5354	–	–	–	–
NGC 5353	–	–	–	–
NGC 5746	1.882	4.403	3.852	0.812
	0.116	0.107	0.096	0.067
NGC 5908	–	–	–	–
NGC 5987	–	–	–	–

good agreement for the slopes of the correlations, there are offsets between studies. Such offsets may result from differences in calibration to the Lick system, differences in aperture size and/or orientation, and systematic differences in velocity dispersion estimates. Values of indices in the early-type galaxies of our sample are also shown in Fig. 3. Correlations from the fully calibrated K00 study of Fornax cluster galaxies (shown as thick lines in Fig. 3) most closely match our results, although our sample covers a significantly narrower range of velocity dispersion than the K00 sample (a result of our selection of *bright*, nearby ellipticals).

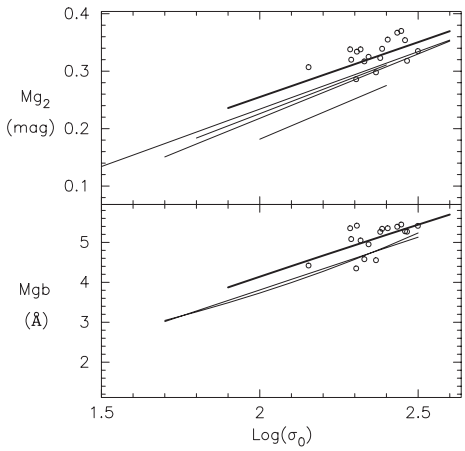

Figure 3. Mg_2 and Mgb with central velocity dispersion (σ_0 in km s^{-1}). Circles show our E and S0 galaxies. The thick line shows the mean trend from K00. Thinner lines show trends from other authors as detailed in the text. N.B. Both Trager et al. (2000b) and K00 estimated correlations on a log(index) scale, resulting in the curvatures in these plots.

In Fig. 4 we show plots of selected metallicity-sensitive indices from the blue spectra against log velocity dispersion for our galaxy sample. Indices omitted are those most severely affected by the dichroic response problem outlined in Sections 2.3 and 2.4.2. Table 5 details the fits (minimizing χ^2) of indices against velocity dispersion for both early- and late-type galaxies in our sample. Values given are from fits with *y*-axis errors only (which dominate in most cases). Errors in slope and intercept are taken as half the difference between the fit using index errors for χ^2 minimization and that using velocity dispersion errors. From Table 5 it can be seen that in the metallicity-sensitive indices of early-type galaxy sample we detect no significant (3σ) slopes. However, our results for Mg_2 and Mgb are consistent with the positive trends with velocity dispersion noted by previous studies (Fig. 3). If we compare the scatter of our Mg_2 and Mgb data about our best-fitting lines (0.02 mag and 0.3 Å respectively) with their scatter about the K00 correlations (Fig. 3), we find no significant difference. We tested the fit of the K00 correlations to our early-type galaxy data for all common indices. For the majority of indices our scatter about the K00 correlations is similar to scatter of the K00 data. Consequently, in Fig. 4 we use K00 correlations (shown as thin lines) for all common indices for purposes of comparison to bulges.

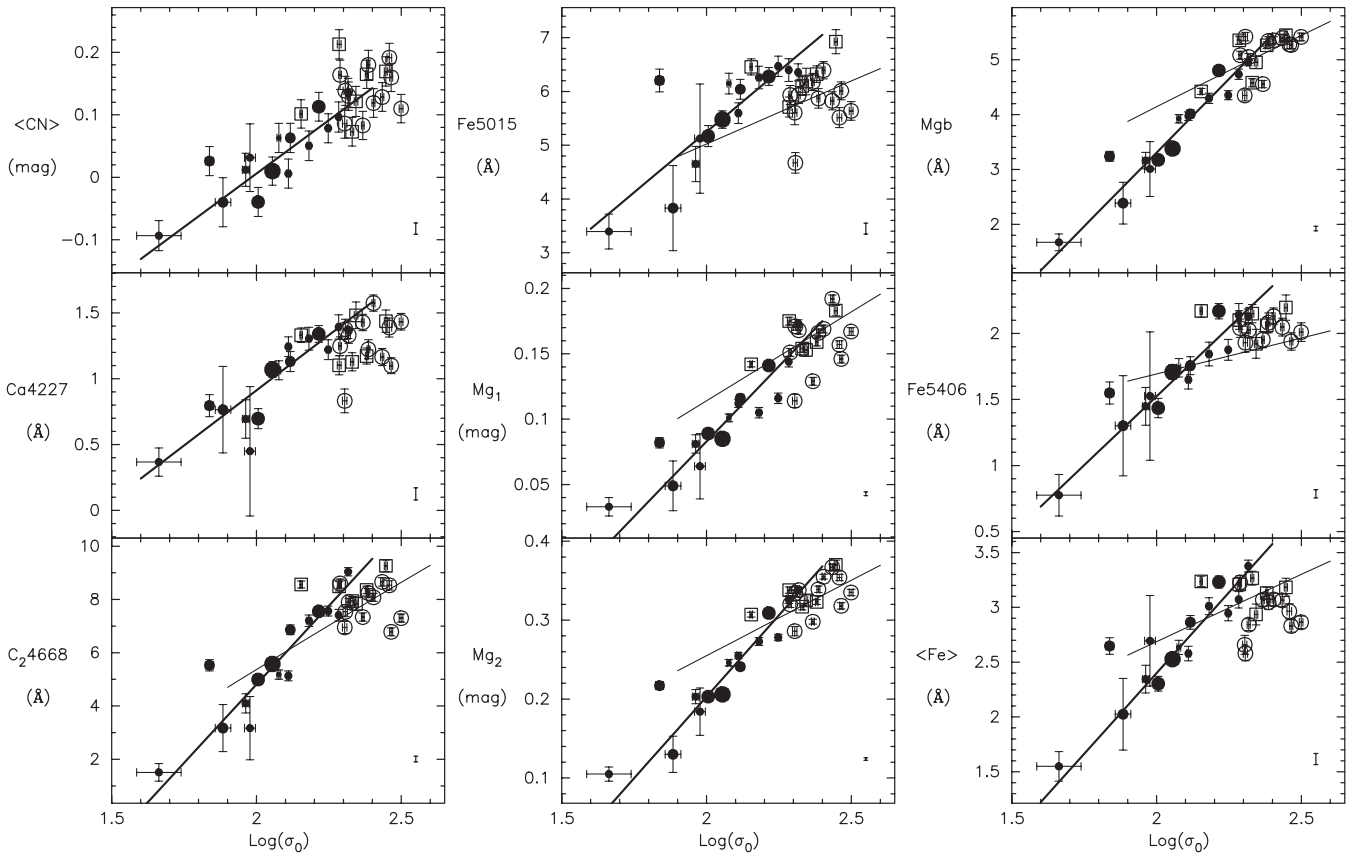

Figure 4. Central metallicity-sensitive indices plotted against logarithm of central velocity dispersion (σ_0 in km s^{-1}). Thick lines are fits to our spiral bulge data (solid symbols with symbol size largest for S0/a and smallest for Sbc). Open symbols show early-type galaxies (circles for Es and squares for S0s). Thin lines show trends from K00 for early-type galaxies. Error bars include all reduction and calibration errors. Uncertainties in calibration to the Lick system are shown as an isolated error bar at the bottom right of each plot.

Most previous authors report weak or no trends in Fe indices (Fisher et al. 1996; Trager et al. 1998; Jørgensen 1999) with velocity dispersion for early-type galaxies. Within the narrow velocity dispersion range covered by our sample, we echo this finding (Fig. 4 and Table 5). However, K00 found correlations for all the metallicity-sensitive indices he observed. We note the possibility that such correlations would have been present in our data had the velocity dispersion range of our study been larger. For Fe5406 we find values consistently above the K00 correlation.

Table 5. Correlations between indices and velocity dispersion. The number of galaxies (N) in the fit, slopes, intercepts, (un-weighted) correlation coefficients (r) and χ^2 for best-fitting correlations are given. Derivation of errors (given in brackets) are described in the text. For Mg_2 and Mgb in early-type galaxies, the correlations of K00 are also given. N.B. For Mgb the K00 correlation has been transformed from magnitudes (as presented in K00) to Ångströms used in this work. NGC 4313 was omitted from correlations for late-type galaxies (see Section 3.2.2).

Index	N	dI/d(log σ_0)	Intercept	r	χ^2
EARLY-TYPE GALAXIES					
Ca4227	17	0.22(9.36)	0.76(22.03)	0.21	97
Fe5015	17	−0.50(30.18)	7.17(71.08)	0.02	105
Fe5270	17	−0.84(3.13)	5.18(7.38)	−0.16	108
Fe5335	17	−0.62(3.10)	4.32(7.30)	−0.18	66
⟨Fe⟩	17	−0.72(2.50)	4.73(5.90)	−0.19	137
Fe5406	15	−0.38(1.27)	2.95(3.00)	−0.21	18
CN_1	17	0.086(0.855)	−0.089(2.013)	0.19	21
CN_2	17	0.113(0.741)	−0.107(1.745)	0.23	26
⟨CN⟩	17	0.099(0.792)	−0.098(1.866)	0.21	47
$C_2$4668	17	−1.99(13.45)	12.73(31.68)	−0.12	218
Mg_1	17	0.066(0.216)	0.003(0.510)	0.35	438
Mg_2	17	0.114(0.178)	0.062(0.419)	0.51	392
K00 Mg_2	13	0.191(0.023)	−0.127(0.054)		
Mgb	17	2.68(1.76)	−1.24(5.39)	0.61	245
K00 Mgb	13	2.60(0.40)	−1.06(1.36)		
$H\delta_A$	17	−2.11(20.71)	2.61(48.70)	−0.24	29
$H\delta_F$	17	−1.26(3.32)	3.05(7.80)	−0.43	40
$H\gamma_A$	17	−2.83(44.85)	1.04(105.53)	−0.19	29
$H\gamma_F$	17	−1.66(31.03)	2.66(73.04)	−0.21	10
$H\beta$	17	−1.74(0.66)	5.68(1.56)	−0.71	49
CaT	13	−2.35(1.94)	13.31(4.51)	−0.53	52
Mg I	13	−0.28(0.86)	1.40(2.00)	−0.51	16
LATE-TYPE GALAXIES					
Ca4227	14	1.68(0.22)	−2.44(0.48)	0.90	21
Fe5015	14	4.51(0.34)	−3.77(0.75)	0.95	21
Fe5270	14	3.03(0.14)	−3.46(0.30)	0.93	19
Fe5335	14	2.86(0.57)	−3.50(1.26)	0.92	35
⟨Fe⟩	14	2.95(0.24)	−3.49(0.52)	0.96	40
Fe5406	14	2.09(0.23)	−2.65(0.48)	0.97	24
CN_1	14	0.337(0.088)	−0.687(0.190)	0.92	6
CN_2	14	0.347(0.093)	−0.669(0.202)	0.91	8
⟨CN⟩	14	0.340(0.089)	−0.683(0.193)	0.91	10
$C_2$4668	14	11.80(1.53)	−18.78(3.39)	0.96	84
Mg_1	14	0.230(0.042)	−0.377(0.091)	0.94	155
Mg_2	14	0.413(0.027)	−0.623(0.060)	0.97	170
Mgb	14	5.37(0.22)	−7.43(0.48)	0.98	70
$H\delta_A$	14	−12.34(1.93)	25.72(4.18)	−0.93	24
$H\delta_F$	14	−6.04(0.08)	13.80(0.17)	−0.95	38
$H\gamma_A$	14	−14.33(2.00)	26.41(4.40)	−0.88	24
$H\gamma_F$	14	−7.04(1.63)	14.68(3.59)	−0.84	10
$H\beta$	9	−1.44(0.74)	5.09(1.64)	−0.81	16
CaT	12	−1.03(5.88)	10.25(12.06)	0.28	50
Mg I	12	0.39(0.31)	−0.12(0.63)	0.78	9

However, the side-bands of this index lie in a region of our spectra where vignetting effects are beginning to appear. Consequently, it is possible that a small undetected systematic effect may be biasing this index in our results. Previous authors have reported that the calcium indices (Ca4227 and Ca4455) follow similar trends to Fe indices, rather than the trends in enhanced indices such as Mg_2 (Vazdekis et al. 1997; Trager et al. 1998). We again echo this finding within the narrow range of velocity dispersions of our sample.

Plots of age-sensitive indices with velocity dispersion are shown in Fig. 5. In early-type galaxies no significant trends with velocity dispersion are evident in the Hδ and Hγ indices. However, for the Hβ index a $\sim 3\sigma$ correlation is found (Fig. 5 and Table 5). The slope of this weak correlation is steeper than that found by K00 [dHβ/d(log σ) ~ -0.4], which is shown as a thin line in Fig. 5. The presence of such a correlation in the highly age-sensitive Hβ index, while the more degenerate Hδ and Hγ indices show no correlations, suggests the presence of a trend of increasing age and/or decreasing metallicity with velocity dispersion in the early-type galaxies.

S0 galaxies, shown as open squares in Fig. 4, follow similar trends to elliptical galaxies in all indices. The similarity in

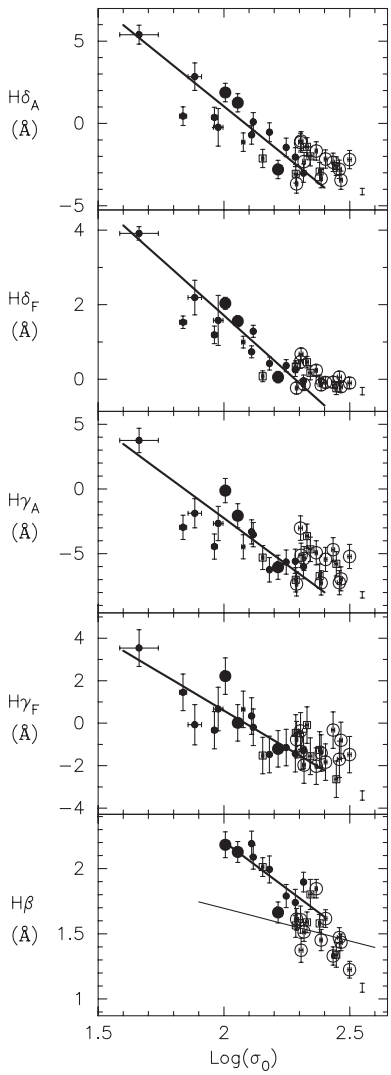

Figure 5. Age-sensitive indices against logarithm of central velocity dispersion. Symbols and errors as in Fig. 4.

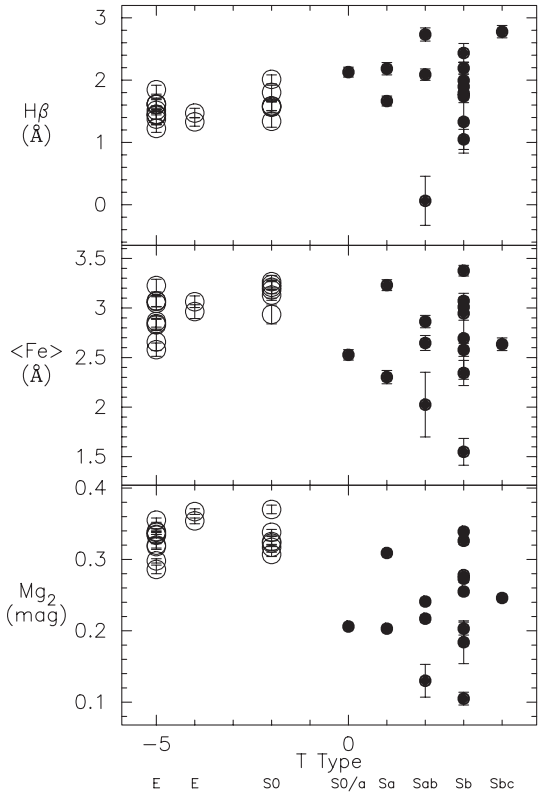

Figure 6. Central indices with Hubble (T) type. Open symbols are early types and filled symbols are late types.

indices in E and S0 types can also be seen in Fig. 6, where the values of key indices are compared for all Hubble types. In this plot, indices show no correlation with Hubble type for spiral bulges.

3.2.2 *Late-type galaxies*

All metallicity-sensitive indices in the blue spectra of our late-type galaxy sample show strong correlations with velocity dispersion (Fig. 4 and Table 5), including those not shown in Fig. 4. One outlier to these trends for late-type galaxies is NGC 4313, which exhibits a strong central depression in $\log \sigma$. This galaxy has been omitted from the line-fitting procedure. The highest velocity dispersion bulges show index values coincident with those of early-type galaxies. Indeed, for all indices in our sample, early and late types form a continuous locus in the index–velocity dispersion plane. However, the slopes of the correlations in late-type galaxies are significantly steeper than those found by K00 for early-type galaxies (Fig. 4). In general, the scatter about the correlations of late-type galaxies is also smaller than that of early types. Anticorrelations with velocity dispersion are also evident among the late-type galaxies in all age-sensitive indices (Fig. 5) with low velocity dispersion bulges having stronger hydrogen absorption lines (aberrant emission-line galaxies detailed in Section 2.5.2 are omitted from line fitting in the case of Hβ). The strong trends of both metallicity- and age-sensitive indices with velocity dispersion in late-type galaxies suggests that SFH is closely associated with the depth of potential well in the centres of bulges.

3.2.3 *Red data*

CaT (the sum of Ca II at 8498 and 8542 Å) and Mg I are plotted against velocity dispersion in Fig. 7. Trends with velocity dispersion are not as clear in these indices. In early-type galaxies, the Mg I index shows behaviour with velocity dispersion different from that of the Mg_1, Mg_2 and Mgb indices in the blue. However, it is difficult to make direct comparisons because, as previously suggested (Section 3.1), NIR indices may be sampling different stellar populations from those sampled by blue indices.

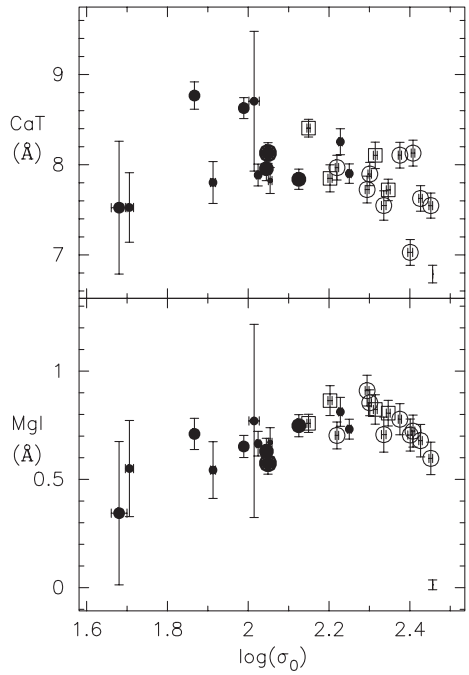

Figure 7. CaT and Mg I against central velocity dispersion. Symbols and errors as in Fig. 4.

3.2.4 *Potential disc contamination of late-type galaxies*

Early- and late-type galaxies in our sample exhibit similar index values in the region where their velocity dispersions overlap ($150-200\,\mathrm{km\,s^{-1}}$). However, towards lower dispersions, bulges lie systematically further from the K00 trends for early-type galaxies (Fig. 4). It was a concern that this behaviour may be the result of disc contamination. Khosroshahi, Wadadekar & Kembhavi (2000) carried out bulge-disc decomposition of a number of edge-on ($i > 50°$) spiral galaxies. They show that for Hubble types earlier than Sbc ($T < 4$) the bulge-to-disc central luminosity ratio always exceeds 10, i.e., no more than 10 per cent of the observed light originates in the disc. They also show that this ratio increases to ~ 1000 in the case of Sa galaxies. The worst-case assumption for metallicity-sensitive indices is that of a smooth continuum contribution from the disc. Under such circumstances, a maximum reduction of ~ 10 per cent is expected for both line and molecular-band indices. We compare the K00 correlations for metallicity-sensitive indices in early-type galaxies with our correlations for late types in Table 6. Values of indices on the correlations are given, for our bulge data and the K00 correlations, at $\log \sigma_0 = 2.0$ (mid-range value for bulges). Percentage differences between the two correlations can be seen to vary from -27 to $+5$ per cent. Clearly, the difference can not be modelled by the simple addition of continuum to the bulge light. It should also be noted that, for the Mg indices, a minimum bulge contribution of ~ 25 per cent is required to account for the differences between correlations. This is well in excess of the 10 per cent maximum expected from

Khosroshahi et al. (2000), and the difference increases at velocity dispersions less than 100 km s^{-1}. We also note that there is no evidence that the indices of late-type galaxies correlate with Hubble type (Fig. 6), as might be expected if significant disc contamination were present.

We therefore conclude that while metallicity-sensitive indices could be depressed by as much as 10 per cent by disc contamination, this effect is not evident in our data, nor can it explain the observed differences between correlations in early- and late-type galaxies.

3.3 Diagnostic index plots

In this section we compare the results of our index determinations to the values predicted for SSPs. We use V99 SSPs for our analysis. These (web-published) SSPs are based on Bertelli et al. (1994) isochrones (as detailed in V96), and Vazdekis (1999a) transformations to the observational plane. We use V99 SSPs rather than those of W94 and Worthey & Ottaviani (1997), as V99 make use of the more up-to-date and complete isochrones of Bertelli et al. (1994). V99 also includes the CaT and Mg I indices in their calculations of SSP index values. Metallicities derived from degeneracy-breaking diagnostic plots using V99 SSPs are generally higher by $\sim$0.1 dex than those implied by W94 SSPs. For galaxies older than $\sim$5 Gyr, V99 SSPs also imply ages younger by $\sim$0.15 dex.

The $\langle$Fe$\rangle$ versus Mg_2 diagnostic plot is shown in Fig. 8. This plot clearly shows the enhancement of the Mg_2 index (or, equivalently, the deficiency in the $\langle$Fe$\rangle$ index) in early-type galaxies with respect to solar abundance ratio SSPs. The plot also demonstrates the age/metallicity degeneracy of these two indices. The grid includes SSPs ranging from 1.5 to 17 Gyr in age and with metallicities ([Fe/H]$_{SSP}$) covering the range [Fe/H]$_{SSP} = -1.7$ to $+0.5$. The good agreement between our data and the correlation of Gorgas et al. (1997) for early-type galaxies is also illustrated. Late-type galaxies seem to span the SSP grid. This echos the tentative finding of our previous study (Proctor et al. 2000) that late-type galaxies exhibit abundance ratios closer to solar than those found in elliptical galaxies. The four bulges observed by Proctor et al. were not fully calibrated to the Lick system due to a lack of observations of suitable calibration stars. However, we note that most fully calibrated studies find that small positive corrections are required to compensate Mg_2 for the lack of flux calibration in the Lick observations, while Fe5270 and Fe5335 require only very small corrections (e.g. Worthey & Ottaviani 1997; K00). The Lick offsets given in Table 2 for the present data set were thus applied to the Proctor et al. data. The Sa galaxy NGC 3623 was observed in both studies. The two independent values for both Mg_2 and $\langle$Fe$\rangle$ in this galaxy were within errors. Consequently, this galaxy was not included when the results of the Palomar study were added to Fig. 8 (solid squares). Additional errors of 0.01 mag and 0.04 Å have been added in quadrature to the Proctor et al. errors for Mg_2 and $\langle$Fe$\rangle$ respectively to allow for uncertainty in the corrections to the Lick system.

Given the tendency, reported by previous authors, for Ca indices to follow similar trends to Fe indices (Vazdekis et al. 1997; Trager et al. 1998), the NIR CaT and Mg I indices allow plotting of a diagnostic plot similar to $\langle$Fe$\rangle$ versus Mg_2 in the blue. This diagnostic plot (CaT versus Mg I) is also shown in Fig. 8. In this figure, early-type galaxies lie within with the SSP grid. A simplistic interpretation would be that this indicates [Mg/Ca] = 0 and, assuming that Ca follows the same trends as Fe, a value [Mg/Fe] = 0. However, when these indices are plotted against age-sensitive indices (e.g., Hβ), problems with the Mg I index become apparent (Section 3.3.1) and this interpretation can not be sustained.

Table 6. Index values from correlations at $\log(\sigma_0) = 2.0$. The percentage difference between the values from the two correlations is also given.

Index	K00	Spirals	per cent
$C_2$4668	5.37	4.81	-10 per cent
Fe5015	5.02	5.25	$+5$ per cent
Mg_1	0.114	0.083	-27 per cent
Mg_2	0.255	0.194	-24 per cent
Mgb	4.14	3.31	-20 per cent
Fe5406	1.69	1.52	-10 per cent
$\langle$Fe$\rangle$	2.69	2.40	-10 per cent

3.3.1 *Breaking the degeneracy*

Plots that most clearly break the age/metallicity degeneracy are

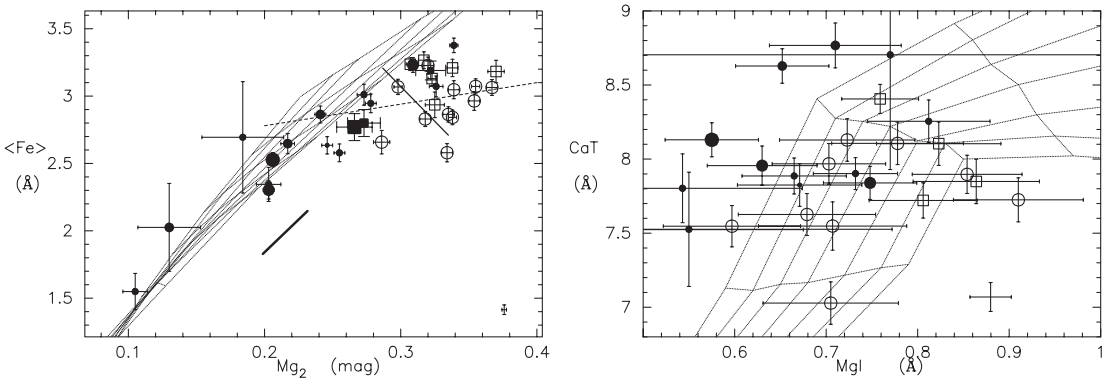

Figure 8. $\langle$Fe$\rangle$ versus Mg_2 (left) for our WHT data and three galaxies from Proctor et al. (2000) (solid squares). Values for a fourth galaxy from Proctor et al. (NGC 3623) agree (within errors) with values from the WHT observation. All other symbols are as in Fig. 4. Grid lines show V99 solar abundance ratio SSPs at ages of 1.5, 2, 3, 5, 8, 12 and 17 Gyr and [Fe/H]$_{SSP}$ of -1.7, -1.0, -0.5, -0.25, 0.0, $+0.25$, and $+0.5$ dex. In the left-hand plot the dashed line shows the correlation of Gorgas et al. (1997) for early-type galaxies, which is consistent with our data. The thick solid line shows the range of index values covered by the primordial collapse models described in Section 5.1, while the short, thinner solid line shows the range of values covered by the merger models in Section 5.3. Error bars at the bottom right of each plot refer to errors incurred in calibrating on to the Lick system.

shown in Figs 9 and 10. These plots show metallicity-sensitive indices against Hβ, and compare galaxy values to V99 SSP predictions. We show indices against Hβ, since this is the most age-sensitive index and other age-sensitive indices (H$\delta_{A,F}$, G4300 and H$\gamma_{A,F}$) are among those effected by the dichroic response problem in our data.

The Hδ and Hγ indices were also not among the indices whose sensitivities to element abundance ratios were modelled by TB95. Fig. 9 shows indices sensitive to Fe on the left, while indices sensitive to abundance ratios are shown on the right. Early-type galaxies in Fig. 9 exhibit different trends in Fe and abundance-ratio-sensitive indices. In these galaxies, the *increasing* Hβ with line-strength in Fe indices contrasts with the *decreasing* Hβ with line-strength in abundance ratio sensitive indices. The trend in Fe indices suggests that Fe abundance is anticorrelated with age in early-type galaxies, while the growing disparity between Fe and

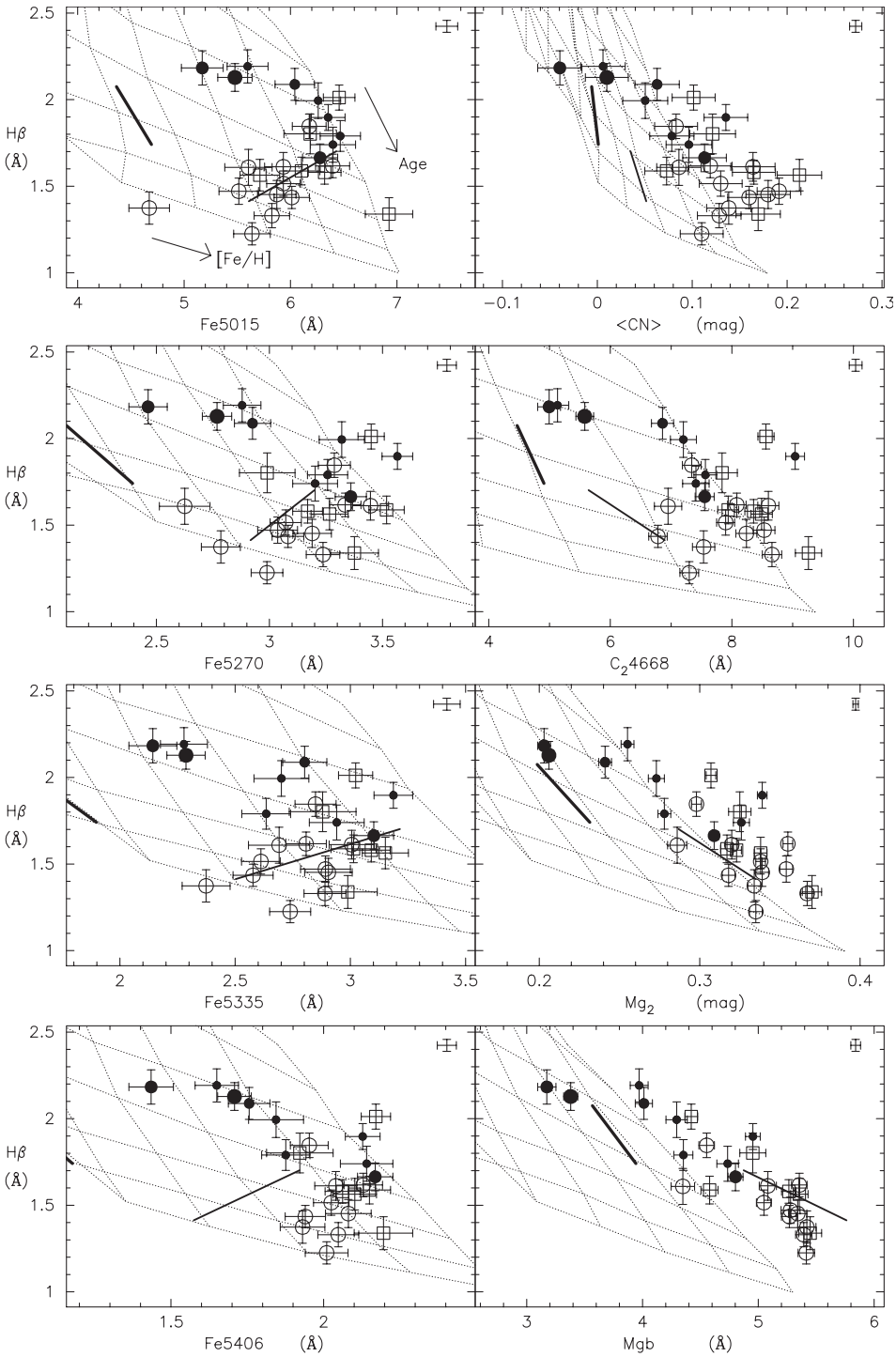

Figure 9. Metallicity-sensitive indices plotted against Hβ. Symbols as in Fig 4. Fe indices are shown on the left, while indices sensitive to Mg and C abundance ratios are shown on the right. The uncertainty in calibration to the Lick system is shown at the top right of each plot. Short, thick and thinner lines show primordial collapse and merger models respectively. These and the grid lines are as in Fig. 8.

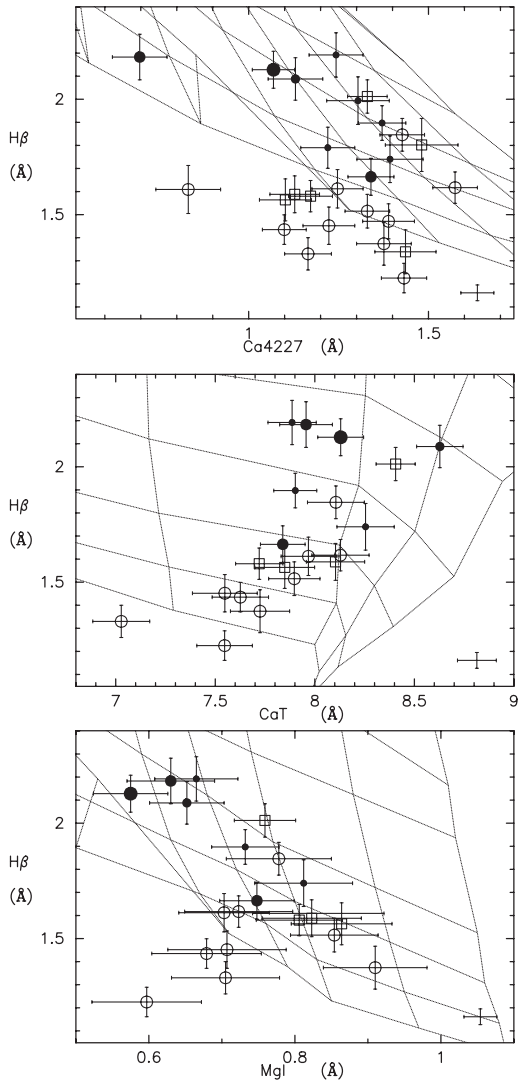

Figure 10. Calcium-sensitive indices; Ca4227 (top) and NIR CaT (middle) plotted against Hβ. Also shown is the Mg I index (bottom) against Hβ. The uncertainty in calibration to the Lick system is shown at the bottom right of each plot. Symbols as in Fig. 4.

abundance ratio sensitive indices suggests increasing abundance enhancement in light elements with age.

In late-type galaxies, Hβ *decreases* with all metallicity-sensitive indices in the blue (Fig. 9). The position of these galaxies with respect to the SSP grids is also more consistent between plots of Fe indices and those sensitive to abundance ratios. This reflects abundance ratios closer to solar in these objects, as noted in Proctor et al. (2000). The positions of late-type galaxies also suggests that the populations are relatively young (luminosity-weighted ages ≤ 5 Gyr) with a wide range of metallicities.

Fig. 10 shows a plot with Hβ of the blue Ca4227 (top plot). Comparison of this plot with Fig. 9 shows the similarity in behaviour of Ca and Fe indices previously reported (Vazdekis et al. 1997; Trager et al. 1998), with Ca4227 suggesting lower metallicities at increased age. Also shown in Fig. 10 are the NIR CaT and Mg I indices plotted against Hβ. A note of caution here is that we are comparing indices derived from NIR spectra with Hβ derived from the blue spectra. As previously noted, we suspect that the two wavelength ranges may be sampling differing populations. However, under the assumption that the differences in age and metallicity of the populations sampled by NIR and blue wavelength bands are reasonably small and uniform across our galaxy sample, we attempt to interpret these diagrams.

The CaT index again shows the similarity in behaviour of Ca and Fe indices. That is, the trend of increasing Hβ with CaT is similar to those exhibited by blue Fe indices. However, in the Mg I–Hβ plot, while some galaxies retain the behaviour of blue Mg indices, many galaxies are displaced to extremely low metallicities when compared to the SSP grids. These galaxies tend to be both the oldest, and have the highest velocity dispersion. However, Mg I is a weak index, prone to measurement problems; therefore further observations of Mg I are needed to ascertain its behaviour relative to SSPs. We therefore draw no strong conclusions from either the Mg I–Hβ or the Mg I–CaT plots.

4 ESTIMATION OF AGE, METALLICITY AND ABUNDANCE RATIO ENHANCEMENT

Our aim is to use the indices of solar-neighbourhood abundance ratio SSPs as the basis for estimating luminosity-weighted ages, metallicities and abundance ratios of galaxies. This requires us to estimate the effects on indices of the non-solar abundance ratios observed in many galaxies (e.g. Davies et al. 1993). Thus we aim to construct grids of SSPs with varying age, $[Fe/H]_{SSP}$ *and* abundance ratio for comparison with observations. This requires knowledge/estimation of:

(1) the abundance ratio pattern in the local stars used to construct SSPs;

(2) the difference between the local abundance ratio (SSP) pattern and that in the galaxy populations being studied;

(3) the effects such a difference would have on photospheric conditions (surface gravity ($\log g$), effective temperature ($T_{\rm eff}$) and luminosity) in whole populations, i.e., the effects on isochrones, and

(4) the effects of differences in abundance ratios on the strength of individual indices in stars, assuming fixed photospheric conditions.

Armed with the above, it is possible to estimate corrections to the indices of solar abundance ratio SSPs for non-solar abundance ratios, for comparison with observations. The above points are discussed in turn below.

4.1 The local abundance pattern

Stellar metallicity estimates, used in the construction of both W94 and V99 SSPs, were based on analysis of solar-neighbourhood stars (e.g. Edvardsson et al. 1993 in V99; Hansen & Kjærgaard 1971 and Gustafsson, Kjærgaard & Andersen 1974 in W94). The wavelength ranges used generally contain a large number of Fe lines, thus providing good estimates of iron abundance [Fe/H]. However, solar-neighbourhood stars possess considerable scatter in the abundance ratios of individual elements. In high-metallicity stars ([Fe/H] $\geq$ solar) abundance ratios show moderate scatter about solar values (Edvardsson et al. 1993; Feltzing & Gustafsson 1998). Thus, for SSPs, the calibration of which averages a large number of local stars, we may assume $[Z/H]_{SSP} = [Fe/H]_{SSP}$ for $[Fe/H]_{SSP} \geq 0$. On the other hand, solar-neighbourhood stars with [Fe/H] < 0 exhibit non-solar abundance patterns, with α-elements (e.g., O, Ne, Na, Mg, Al, Si, S, Ar, Ca) enhanced with respect to Fe peak elements (e.g., Fe, Ni, Cr) (Ryan, Norris & Bessell 1991;

Edvardsson et al. 1993; Feltzing & Gustafsson 1998; Idiart & Thévenin 2000). The α-element abundances are also enhanced with respect to C, which has solar abundance ratio (or below) down to very low metallicities (Ryan et al. 1991). Abundance ratios of α-elements [α/Fe] in these stars increase linearly from [α/Fe] ~ 0.0 at [Fe/H] $= 0.0$ to [α/Fe] $\sim +0.3-0.5$ (depending on the element concerned) at [Fe/H] $= -1$. Moderate scatter in the abundance ratios of individual elements about these trends is again observed. As SSPs with $[\mathrm{Fe/H}]_{\mathrm{SSP}} < 0$ are therefore based on stars with non-solar abundance ratios, we assume that $[\mathrm{Fe/H}]_{\mathrm{SSP}}$ more closely approximates [Fe/H] in the stars than [Z/H]. Thus, in low-metallicity SSPs (and any other non-solar abundance ratio population) we must assume a relationship between [Z/H], [Fe/H] and [E/Fe] (where E is the mass of all elements with enhanced abundance ratios – see Table 7, column 3). As non-linear effects are small (Tantalo, Chiosi & Bressan 1998), and following T00a, we assume a linear relationship:

$$[Z/H] = [Fe/H] + A[E/Fe], \tag{3}$$

the differential form of which,

$$\Delta[Z/H] = \Delta[Fe/H] + A\Delta[E/Fe], \tag{4}$$

may be used to derive estimates of the factor A in low-metallicity stars by comparing a solar composition with one in which all α-elements are doubled in abundance ([Fe/H] $= 0$, [E/Fe] $= +0.301$). From the values given in Table 7 it can be seen that α-elements constitute 70 per cent of metals at solar abundance ratio. Doubling all these elements therefore gives Δ[Z/H] $= +0.25$ [assuming $\Delta Y = 2.2\Delta Z$ (Lebreton et al. 1999) and an internally consistent handling of H]. This yields an estimate of $A = 0.83$. Non-linear effects and uncertainties in the handling of He result in an uncertainty in the value of A of approximately ± 0.06. For solar-neighbourhood stars we characterize the trend in [E/Fe] with [Fe/H] in the range $-1 \leq$ [Fe/H] < 0 by

$$[E/Fe] = -0.45[Fe/H]. \tag{5}$$

The value 0.45 in equation (5) is the overall enhancement in α-element abundances with respect to solar in the data of Salasnich et al. (2000) for low-metallicity field stars. Combining equations (3) and (5), we get

$$[Z/H] = 0.63[Fe/H]. \tag{6}$$

We use this equation to estimate $[\mathrm{Z/H}]_{\mathrm{SSP}}$ in SSPs with $-1 \leq [\mathrm{Fe/H}]_{\mathrm{SSP}} < 0$.

Table 7. Mass of individual elements as a fraction of total metals $(X_i/Z)_\odot$ in the Sun. Data are from Cox (2000). The total mass fraction of metals in the Sun ($Z_\odot$) is assumed to be 0.0189. Elements enhanced in low-metallicity, solar-neighbourhood stars and in galaxy populations are identified by a +. These are the elements which are included in the enhanced group (E) in each case. The final column indicates (with Y) the elements modelled by TB95. The last row in the second column shows the total fraction of all tabulated elements in the Sun. For the other three columns, totals indicate solar proportions of elements identified by + or Y.

Element	$(X_i/Z)_\odot$	Low [Fe/H] stars	Galaxy populations	Modelled by TB95
C	0.1619		+	Y
N	0.0583		+	Y
O	0.5054	+	+	Y
Ne	0.0921	+	+	
Na	0.0018	+	+	Y
Mg	0.0343	+	+	Y
Al	0.0030	+	+	
Si	0.0370	+	+	Y
S	0.0193	+	+	
Ar	0.0054	+	+	
Ca	0.0034	+		Y
Cr	0.0009			Y
Fe	0.0719			Y
Ni	0.0039			
Total	0.9986	0.7017	0.9185	0.8749

4.2 Abundance ratio patterns in galaxies

Given the well-known overabundance of Mg with respect to Fe in elliptical galaxies (e.g. O'Connell 1976; Worthey et al. 1992), one approach to modelling abundance ratios in galaxies would be to use the pattern observed in low-metallicity, solar-neighbourhood stars which show a similar enhancement in Mg. However, while galaxy studies show Mg-sensitive indices (Mg_1, Mg_2 and Mgb) to be enhanced with respect to Fe indices such as Fe5227 and Fe5335 (Gorgas et al. 1997; Vazdekis et al. 1997; K00; T00a; Fig. 9 in this paper), many of these studies show indices centred on Ca features (Ca4227 and Ca4455) to be unenhanced (see also Fig. 10). This is not the only difference between local, low-metallicity stars and galaxy populations. C-sensitive indices (CN_1, CN_2 and C_24668) are also enhanced in galaxy populations (Vazdekis et al. 1997; K00; Fig. 9 in this paper). The differences between abundance patterns in low-metallicity, solar-neighbourhood stars and that in high-metallicity galaxy populations are interesting, but not surprising given the difference in both metallicity and environment. They do, however, render this approach to modelling galaxy abundance ratios unworkable, as many Lick indices are particularly sensitive to C abundance. Here we make the assumption that enhancement in Mg abundance reflects an equal enhancement in the abundances of all α-elements in Table 7, with the exception of Ca which is assumed to follow Fe−peak element abundances. C is also assumed to be enhanced. For galaxy population abundances we have therefore defined two groups; the 'Fe−like' elements (Ca, Cr, Fe and Ni) and the 'enhanced' elements (C, N, O, Ne, Na, Mg, Al, Si, S and Ar – see Table 7, column 4) with the abundance of each element, in each group, enhanced by the same factor. This is similar to model 4 of T00a, where a similar analysis was carried out (see Section 4.5). The two groups of elements combined represent 99.86 per cent of the mass of metals present in the solar photosphere (Table 7). Using these assumptions, we hope to obtain reasonable estimates of age, metallicity and the degree of enhancement in galaxy populations.

For the three galaxies with estimated [Fe/H] < 0 it is necessary to compensate for the non-solar abundance ratios in the stars used to calibrate the SSPs. We use equation (5) to calculate the stellar enhancement. This is added to the *estimated* enhancement (relative to SSP). Finally, equation (3) and the new value of [E/Fe] are used to obtain [Z/H].

4.3 Non-solar abundance ratio isochrones

Until recently, understanding of the effects of non-solar abundance ratios on stellar populations was poor. However, a desire for a better description of the evolutionary tracks of globular clusters led to the development of theoretical isochrones for α-element-

enhanced populations. Salaris & Weiss (1998) and VandenBerg et al. (2000) modelled isochrones for the abundance pattern in metal-poor field stars which possess enhancements in α-element abundances as detailed in Section 4.1. They show that, at low metallicities ([Z/H] < 0), α-enhanced isochrones are well estimated by solar abundance ratio isochrones of the same [Z/H]. However, they also show that at the highest metallicities in their studies ([Z/H] $\sim$ solar) this no longer holds. Salasnich et al. (2000) modelled α-enhanced isochrones at metallicities similar to those observed in galaxy centres ([Z/H] $\sim 0-0.5$). They show that, at these metallicities, due to low atomic numbers and high ionization potentials, α-elements make relatively small contributions to opacity. Consequently, high-metallicity, α-enhanced isochrones possess a higher $T_{\rm eff}$ than solar abundance ratio isochrones of the same [Z/H]. The resultant isochrones are therefore best approximated by solar abundance ratio isochrones of lower [Fe/H]. Fig. 10 of Salasnich et al. shows that an isochrone for a 10-Gyr-old population, with solar metallicity and an α-enhancement of $+0.45$ (i.e., [Fe/H] $= -0.37$, equation 3), is best modelled by a solar abundance ratio isochrone of metallicity [Fe/H] $= -0.25$. At [Z/H] $= +0.6$ ([Fe/H] $= +0.23$) the effect becomes even more pronounced, such that the α-enhanced isochrone straddles the solar abundance ratio isochrones of [Fe/H] $= +0.0$ and [Fe/H] $= +0.3$. Consequently, an approximate use of the Salasnich et al. isochrones is to assume that the addition of α-elements to high-metallicity populations results in *no* change in the isochrones. Equivalently, the position of the isochrones may be considered to depend upon [Fe/H] in the population rather than [Z/H]. This is clearly only an approximation. However, the Salasnich et al. isochrones suggest that, at high metallicities, it is better than assuming α-enhanced isochrones to be best modelled by solar abundance ratio with the same [Z/H]. Differences in abundance pattern between metal-poor field stars and galaxy populations are not expected to make a significant difference to the behaviour of the isochrones, as the majority of significant contributors to opacity are amongst the elements assumed to show similar abundance ratios in both populations (O, Ne, Na, Mg, Al, Si, S, Ar and Ni), while no other individual elements, including C and Ca, contribute significantly to opacity.

As SSP indices are based on empirical relations for line-strengths versus $T_{\rm eff}$, $\log g$ and [Fe/H] in stars, the results of Salasnich et al. (2000) have a significant impact on the interpretation of SSPs. If it is assumed that isochrone positions (e.g., $T_{\rm eff}$, $\log g$) are dependent on [Z/H], then SSPs with $[{\rm Fe/H}]_{\rm SSP} = [{\rm Z/H}]_{\rm POP}$ (where $[{\rm Z/H}]_{\rm POP}$ is [Z/H] in the galaxy) provide the best match to enhanced populations. If, on the other hand, it is assumed that isochrone position is dependent on [Fe/H], then $[{\rm Fe/H}]_{\rm SSP} = [{\rm Fe/H}]_{\rm POP}$ provides the best match.

4.4 Estimating indices in non-solar abundance ratio stars

TB95 modelled the effects of individually doubling the abundances of 10 key elements in the synthetic spectra of three key stellar types (cool giant, turn-off star and cool dwarf), as well as doubling all elements simultaneously. All models were evaluated at fixed $T_{\rm eff}$ and $\log g$, with values based on a 5-Gyr, solar-metallicity isochrone. TB95 assumed no change in the opacity distribution function when doubling individual elements. This approximation is appropriate, as individual elements contribute little to the opacity. For the doubling of all elements, TB95 again assumed fixed $T_{\rm eff}$ and $\log g$, while an opacity distribution function appropriate for twice solar metallicity was used. The results are presented as variations of the 21 Lick indices modelled, in terms of a standard error, caused by doubling each of the 10 elements. The results of doubling all elements are presented in the same manner. Indices modelled by TB95 include 16 present in our study. TB95 did not, however, model Hδ, Hγ Mg I or CaT. One of the elements modelled by TB95 was Ti. The abundance of this element is enhanced in low-metallicity stars, while its atomic mass lies in the range of the Fe$-$like elements. Consequently, the decision as to whether to include Ti among the enhanced or Fe$-$like indices is difficult. We have therefore not included this (low-abundance) element in our analysis. TB95 is the only published study of this type to date.

The effects of changing abundance ratios can be estimated from the TB95 data by defining $R_{i,X}$; the fractional change in the ith index in the TB95 arrays (e.g., CN_1, CN_2, Ca4227, etc.) when the abundance of the element X (e.g., C/H, N/H) is doubled. The value of the enhanced index (I_i') can then be estimated from the solar abundance ratio value (I_i) by (following T00a):

$$I_i' = I_i[(1 + R_{i,X_1})^{E_{X_1}/\log 2}(1 + R_{i,X_2})^{E_{X_2}/\log 2}\ldots\ldots], \quad (7)$$

where E_X is the change in abundance of element X, i.e., $E_X = \Delta$[X/H]. Doubling all elements (column 14 of TB95, tables 4 to 6) can be handled in the same way, i.e., $E_Z = \Delta$[Z/H]. It should be noted that the doubling of all elements in TB95 did not model a simple doubling of the stellar metallicity, as the TB95 calculations were made assuming *fixed* photospheric conditions ($T_{\rm eff}$, $\log g$).

4.5 Constructing non-solar abundance ratio SSPs

It is possible to estimate the effects of non-solar abundance ratios in populations by modelling SSPs as combinations of the cool giant/turn-off/cool dwarf stellar types of TB95. The luminosity-weighted sum of the factors in tables 4 to 6 of TB95, allows estimation of $R_{i,X}$ values for SSPs. These can then be combined, by use of equation (7), to estimate the sensitivities of indices in SSPs to enhancement of elements in the chosen abundance ratio pattern. T00a and Trager et al. (2000b) used a 53/44/3 percentage luminosity-weighted combination of the three stellar types to simulate SSPs. Though not detailed in their paper, the 53/44/3 combination is consistent with values given by W94 for the relative contributions of these stellar types to 3–17 Gyr SSPs of $[{\rm Fe/H}]_{\rm SSP} \sim 0$. The similarity in the sensitivities (in percentage terms) of cool giant and turn-off stars make the results fairly robust to any reasonable combination. We have therefore adopted the T00a luminosity weightings throughout this paper for ease of comparison. Fractional changes in indices for doubling individual element abundances, and doubling [Z/H], for this combination of stellar types, are given in Table 8. The sensitivities of indices to individual elements divides them into two groups: those with sensitivities to individual elements significantly larger than their sensitivity to Z (CN_1, CN_2, G4300, $C_2$4668, Mg_1 and Mgb), and those whose sensitivities to individual elements are similar to or less than their sensitivity to Z (the rest). It is interesting to note that the strong sensitivities of the first group are mainly to C and Mg, both of which are enhanced elements in galaxy populations (see, e.g., Fig. 9, right-hand side). Consequently, in galaxies, these indices are dominated by abundance ratio effects rather than [Z/H].

The next step in constructing non-solar abundance ratio SSPs is to select the SSP whose isochrone best matches that expected in the population under study. It is to the indices of this SSP that the TB95 corrections for non-solar abundance ratios are applied. On the basis of the isochrone models available at the time (Salaris & Weiss

Table 8. Fractional changes ($R_{i,X}$) in index values of 53/44/3 mix when abundances of individual elements (e.g., C/H) are doubled. These data are derived from tables 4 to 6 of TB95, and are shown here to illustrate the sensitivities to individual elements.

Index	C	N	O	Mg	Fe	Ca	Na	Si	Cr	Ti	Z
CN_1	1.75	0.54	−0.46	−0.13	−0.03	−0.07	−0.03	0.11	−0.10	0.03	0.40
CN_2	1.09	0.35	−0.29	−0.10	−0.03	−0.05	−0.02	0.12	−0.05	0.03	0.29
Ca4227	−0.32	−0.05	0.10	0.00	0.05	0.31	−0.01	0.00	−0.01	0.00	0.24
G4300	0.27	0.00	−0.06	−0.02	−0.04	0.01	−0.01	−0.01	−0.02	0.05	0.04
Fe4383	0.08	−0.00	−0.02	−0.05	0.20	−0.03	−0.01	−0.04	0.00	0.02	0.12
Ca4455	−0.05	−0.01	0.01	−0.01	−0.08	0.00	−0.01	−0.00	0.07	0.03	0.16
Fe4531	0.00	0.01	0.01	−0.01	0.03	0.00	0.01	−0.05	0.04	0.11	0.14
C_24668	1.90	0.00	−0.27	−0.06	0.03	−0.01	−0.01	−0.12	−0.02	0.04	0.36
Hβ	0.03	0.00	−0.00	−0.04	0.00	0.00	0.01	0.01	−0.04	0.00	−0.00
Fe5015	−0.00	0.00	−0.00	−0.10	0.09	0.01	0.01	−0.03	−0.02	0.08	0.14
Mg_1	0.78	−0.00	−0.11	0.26	−0.10	−0.01	−0.01	−0.05	−0.01	0.02	0.21
Mg_2	0.11	−0.01	−0.03	0.23	−0.04	−0.01	−0.01	−0.03	−0.01	0.02	0.14
Mgb	−0.17	−0.01	−0.00	0.37	−0.07	−0.00	−0.01	−0.04	−0.10	−0.01	0.08
Fe5270	0.07	0.01	−0.00	−0.05	0.11	0.02	−0.01	−0.01	0.01	0.02	0.14
Fe5335	−0.05	−0.01	0.01	−0.04	0.20	0.00	−0.01	−0.00	0.03	0.02	0.14
Fe5406	0.03	0.01	−0.00	−0.01	0.17	−0.01	−0.01	−0.00	0.05	0.02	0.15

1998; VandenBerg et al. 2000), T00a assumed that the isochrone position was governed by [Z/H]; thus an SSP with $[Fe/H]_{SSP} = [Z/H]_{POP}$ was selected. However, if we accept the implications of the subsequent Salasnich et al. (2000) study – that isochrone positions are dependent on [Fe/H] rather than [Z/H] – then we must select an SSP with $[Fe/H]_{SSP} = [Fe/H]_{POP}$. Given the uncertainties in this aspect of the modelling, we tested three methods for applying the TB95 data to galaxy observations; the method used by T00a, which assumes isochrone shape to be governed by [Z/H], and two methods designed to be consistent with Salasnich et al. isochrones.

4.5.1 *T00a method*

Given the assumption that isochrone positions are governed by [Z/H], T00a pointed out that there is only one way to achieve the required element abundance ratio enhancements. This involves the reduction in the abundance of Fe− like elements, while enhanced element abundances are (marginally) increased to maintain [Z/H]. Abundances of elements not modelled by TB95 are assumed to remain constant. T00a used equation (4) to derive

$$\Delta[Fe/H] = -A\Delta[E/Fe], \qquad \Delta[Z/H] = 0, \tag{8}$$

where E now refers to all elements enhanced with respect to Fe− like elements in galaxy populations. The data in Table 7, column 4 lead to a value of $A = 0.942$ for the galaxy abundance ratio pattern using the T00a method. From equation (8) this method requires a value of E_X (in equation 7) given by

$$E_X = (1 - A)\Delta[E/Fe], \qquad X = C, N, O, Mg, Na, Si, \tag{9}$$

while for Fe− like indices

$$E_X = -A\Delta[E/Fe], \qquad X = Fe, Ca, Cr. \tag{10}$$

As this method directly estimates age, [Z/H] and [E/Fe], equation (3) is used to calculate [Fe/H]. The difficulty with this method is that it is based on the (now apparently false) assumption that, at the high metallicities observed in galaxy centres, isochrone positions are governed by [Z/H]. None the less, we have applied the T00a analysis to our data using V99 SSPs.

4.5.2 *Methods based on Salasnich isochrones*

In light of the Salasnich et al. (2000) isochrones we chose to test two alternative approaches to the application of TB95 data. As these methods are based on the assumption that, at the high metallicities present in the majority of galaxies, isochrone shape is governed by [Fe/H], we select the SSP with $[Fe/H]_{SSP} = [Fe/H]_{POP}$. We then ensure that the applied enhancements involve no change in the abundance of Fe− like elements. We identify two ways of achieving these requirements with the TB95 data. The first is simply to increase the abundance of each of the elements thought to be enhanced in galaxy populations, while keeping other element abundances constant; the E+ method. For this method, the values of E_X, used in equation (7), are given by:

$$E_X = \Delta[E/Fe], \qquad X = C, N, O, Mg, Na, Si. \tag{11}$$

For other elements and Z in Table 8 $E_X = 0$. As this method is specifically designed to reflect high-metallicity isochrones, it is not used for comparisons with observations of three low-metallicity ([Z/H] < 0) bulges. Instead, for these galaxies we use the T00a method which is consistent with the low-metallicity isochrones of Salaris & Weiss (1998) and VandenBerg et al. (2000). Metallicities and abundance ratios in these three galaxies are transformed to solar scale as described in Section 4.2.

The second approach is to double *all* elements (Z; Table 8) then *reduce* the abundances of Fe− like elements (Fe, Ca and Cr); the Fe− method. This method effectively doubles all elements except those in the Fe− like group. It should again be noted that doubling Z in the tables of TB95 does not represent a simple doubling of the metallicity in a real population, as the TB95 calculations were carried out at fixed $T_{\rm eff}$ and $\log g$, i.e., with no movement of the isochrone. However, this is exactly the requirement of this method, as it assumes that addition of elements whose abundances are enhanced in galaxy populations leaves isochrone positions unchanged. For the Fe− method, the values of E_X used in equation (7) are given by

$$E_X = \Delta[E/Fe], \qquad X = Z, \tag{12}$$

and

$$E_X = -\Delta[E/Fe], \qquad X = Fe, Ca, Cr. \tag{13}$$

Again we have used the T00a method for three bulges with [Z/H] < 0. Despite the differences between T00a and Fe− methods, there are strong similarities, as the fractional changes

Table 9. Comparison of Fe−, E+ and T00a methods for modelling non-solar abundance ratio SSPs. Mean deviations from the best-fitting enhanced SSP models are given (see text for details).

Index	N	Fe−		E+		T00a	
		Mean	χ^2	Mean	χ^2	Mean	χ^2
$H\delta_A$	32	1.1	74	1.9	160	2.1	179
$H\delta_F$	32	1.0	81	2.2	228	2.1	212
CN_1	32	0.5	32	0.4	25	0.1	21
CN_2	32	0.7	53	0.5	38	0.4	38
Ca4227	32	−2.8	378	−3.3	485	−1.7	194
G4300	32	0.2	52	0.1	49	0.1	51
$H\gamma_A$	32	0.6	49	1.1	79	1.0	80
$H\gamma_F$	32	0.3	22	0.6	32	0.5	29
Fe4383	32	0.6	26	0.4	19	0.5	21
Ca4455	32	−1.0	50	−0.6	22	−1.0	44
Fe4531	32	0.2	16	0.3	18	0.4	20
C_24668	32	−0.3	50	−0.9	74	−0.1	39
$H\beta$	26	−1.4	141	0.5	128	−1.2	139
Fe5015	32	−0.6	139	1.2	127	−0.1	109
Mg_1	32	−0.1	102	−2.1	212	−0.1	97
Mg_2	32	1.2	128	1.8	187	1.4	152
Mgb	32	−0.7	89	6.2	1792	−0.8	98
Fe5270	32	0.4	67	−1.4	198	0.7	72
Fe5335	32	0.2	55	−1.6	163	−0.5	70
Fe5406	30	1.9	165	−0.3	24	1.3	91
CaT†	26	−3.2	(507)	−2.8	(376)	−5.5	(1189)
Mg I†	26	6.8	(1374)	6.5	(1287)	6.4	(1229)
Total			1769		4060		1756

† Not included in χ^2 minimizations.

calculated for both methods are dominated by the reduction in Fe− like elements. However, the assumptions regarding isochrones do result in significant differences between estimated ages, as we shall see in Section 4.5.3.

As both E+ and Fe− methods are based on SSPs of known [Fe/H], rather than [Z/H], we must rewrite equation (4) as

$$\Delta[Z/H] = A\Delta[E/Fe], \qquad \Delta[Fe/H] = 0. \tag{14}$$

The data in Table 7, column 4 yield $A = 0.941$ for both E+ and Fe− methods. As both these methods directly estimate age, [Fe/H] and [E/Fe], equation (3) is used to calculate [Z/H].

4.5.3 *Comparison of results from different methods*

For all three methods, grids of non-solar abundance ratio SSPs were generated for [E/Fe] ranging from −0.3 to +0.6 in steps of 0.025 dex. Grid spacings of 0.0125 dex were used for $0.175 \leq \log(\text{Age}) \leq 1.225$ and 0.025 dex for $-0.5 \leq [\text{Fe/H}] \leq 0.75$. Linear extrapolation of the V99 data from [Fe/H] = +0.4 to +0.75 was necessary due to the high Fe index values of a single S0 galaxy (NGC 2549). Indices not modelled by TB95 ($H\delta_A$, $H\delta_F$, $H\gamma_A$ and $H\gamma_F$, Mg I and CaT) were assumed to have no sensitivity to abundance ratio. The best fit (minimum χ^2) was found for each galaxy, for each method. For the six galaxies observed to have aberrant emission (Section 2.5.2), $H\beta$ was omitted from the minimization procedure. The Mg I and CaT indices were also omitted.

Table 9 shows the average deviation (difference between observed and best-fitting non-solar abundance ratio SSP indices, as a multiple of our observational error) and χ^2 values for each index, over all observed galaxies, using each of the three methods. Comparison of best fits for E+ and Fe− methods shows the Fe− method to have a significantly lower total χ^2. We therefore dismiss the E+ method as too unrealistic. The T00a method has marginally

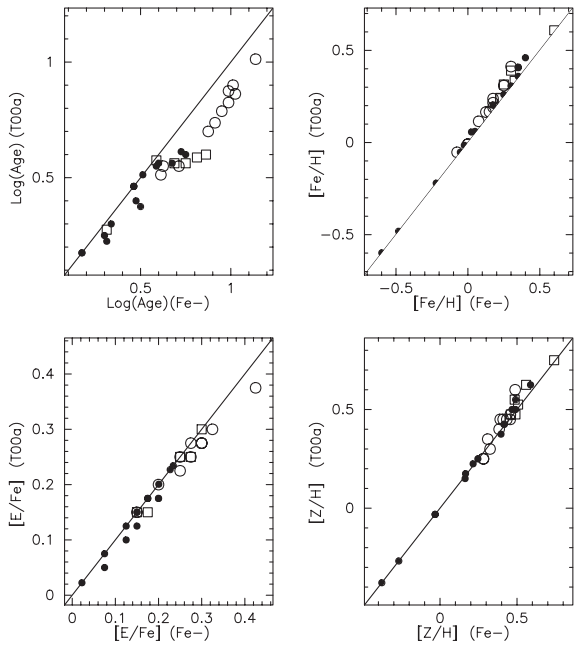

Figure 11. Comparison of results obtained using the T00a method to those using the Fe− method (see Section 4.5). Open circles are elliptical galaxies, open squares are S0s, and filled symbols are late-type galaxies.

lower total χ^2 than the Fe− method. However, this difference hinges on a single index (Ca4227) whose error is underestimated (Section 2.4.2). If this index is excluded, the Fe− method possesses a total χ^2 value ∼12 per cent lower than the T00a method. Comparison of the results for estimates of luminosity-weighted log(Age), [Fe/H], [Z/H] and [E/Fe] from T00a and Fe− methods are shown in Fig. 11. It can be seen that for [Fe/H], [Z/H] and [E/Fe] the results for the two methods are in good agreement. However, the T00a method gives values of log(Age) significantly lower (by ≤0.25 dex) than those derived by the Fe− method. This is a direct result of the difference in assumptions about the effects of non-solar abundance ratios on isochrone positions detailed in Section 4.5. The log(Age) ordering agrees fairly well, to within ∼0.1 dex. Table 10 presents results derived by the Fe− method for all galaxies with [Z/H] > 0, to be consistent with the recent Salasnich et al. (2000) isochrones. For galaxies with [Z/H] < 0 the T00a method has been applied in line with the low-metallicity isochrones of Salaris & Weiss (1998) and Vanden Berg et al. (2000).

As a check on our decision to include all Balmer line indices ($H\beta$, $H\gamma_{A,F}$ and $H\delta_{A,F}$) in the derivation of the values given in Table 10, estimates were also made with differing combinations of these five indices excluded from the fitting procedure. Table 11 details the comparisons of these age/metallicity estimates with those given in Table 10. Also shown are the scatters of the derived values about key correlations identified in Section 3. Offset and scatter in the derived values, when combinations of Balmer lines are excluded from the fitting procedure, are small, with values <0.05 dex in cases when $H\beta$ is not omitted. Indeed, even when all Balmer line indices are omitted, agreement with the values in Table 10 is relatively good. The comparisons presented in Table 11 therefore show that our results are robust to the choice of Balmer lines to include in the fitting procedure. The results even suggest that, with a large number of indices, reasonable estimates can be made *without* the Balmer lines. As many studies have been based on combinations of indices such as $H\beta$, Mg_2 and ⟨Fe⟩, we have also compared results from this combination in Table 11. We find only

Table 10. Central values of luminosity-weighted log(Age), [Fe/H], [E/Fe] and [Z/H] for the 32 galaxies in our sample. Extent of 1σ confidence contours are given as errors (in brackets). Data points with an asterisk are omitted from Fig. 12.

Galaxy	Log(Age)	[Fe/H]	[E/Fe]	[Z/H]
Ellipticals				
NGC2832	0.875(0.069)	0.175(0.050)	0.300(0.025)	0.457(0.074)
NGC2831	0.613(0.069)	0.075(0.050)	0.250(0.038)	0.310(0.085)
NGC3226	1.025(0.056)	−0.075(0.038)	0.425(0.025)	0.325(0.061)
NGC3608	0.950(0.044)	0.125(0.025)	0.275(0.013)	0.384(0.037)
NGC4291	1.013(0.050)	0.000(0.038)	0.300(0.025)	0.282(0.061)
NGC4365	0.988(0.044)	0.175(0.025)	0.250(0.013)	0.410(0.037)
NGC4374	1.138(0.056)	0.000(0.038)	0.300(0.025)	0.282(0.061)
NGC4552	0.988(0.044)	0.150(0.038)	0.325(0.025)	0.456(0.061)
NGC4636	0.913(0.063)	0.175(0.038)	0.275(0.025)	0.434(0.061)
NGC4697	0.712(0.075)	0.300(0.025)	0.200(0.025)	0.488(0.049)
NGC5322	0.625(0.056)	0.250(0.025)	0.150(0.025)	0.391(0.049)
S0s				
NGC2549	0.313(0.113)	0.600(0.075)	0.150(0.013)	0.741(0.087)
NGC3607	0.750(0.056)	0.250(0.025)	0.250(0.025)	0.485(0.049)
NGC4203	0.813(0.063)	0.225(0.038)	0.300(0.025)	0.507(0.061)
NGC4526	0.587(0.038)	0.325(0.038)	0.175(0.025)	0.490(0.061)
NGC5354	0.688(0.113)	0.225(0.062)	0.250(0.038)	0.460(0.098)
NGC5353	0.863(0.081)	0.300(0.050)	0.275(0.025)	0.559(0.074)
Bulges				
NGC2683	0.675(0.088)	−0.025(0.050)	0.200(0.038)	0.163(0.085)
NGC3254	0.587(0.056)	0.025(0.050)	0.150(0.025)	0.166(0.074)
NGC3301	0.338(0.050)	0.175(0.050)	0.075(0.013)	0.246(0.062)
NGC3623	0.725(0.069)	0.300(0.037)	0.125(0.013)	0.418(0.049)
NGC3769	<0.175(0.013)*	−0.576(0.013)*	0.234(0.113)*	−0.356(0.346)*
NGC4157	0.512(0.169)	−0.168(0.138)	0.201(0.087)	0.021(0.220)
NGC4192	0.300(0.056)	0.350(0.038)	0.150(0.025)	0.491(0.061)
NGC4216	0.600(0.025)	0.400(0.025)	0.200(0.025)	0.588(0.049)
NGC4217	0.463(0.363)*	−0.050(0.438)*	0.022(0.275)*	−0.029(0.697)*
NGC4312	0.463(0.213)*	−0.449(0.213)*	0.227(0.237)*	−0.235(0.436)*
NGC4313	<0.175(0.050)*	0.325(0.050)*	0.075(0.038)*	0.396(0.085)*
NGC4419	0.313(0.044)	0.050(0.050)	0.175(0.038)	0.215(0.085)
NGC5746	0.750(0.125)	0.250(0.050)	0.175(0.025)	0.415(0.074)
NGC5908	0.475(0.069)	0.350(0.075)	0.125(0.025)	0.468(0.099)
NGC5987	0.500(0.056)	0.350(0.075)	0.150(0.025)	0.491(0.099)

Table 11. Comparison of results of age/metallicity estimates omitting differing groupings of indices. The average offset and rms scatter about offset (in brackets) are given for each of the derived parameters. Also shown (where appropriate) are the scatters about the most significant correlations detected (see Tables 12 and 13). N.B. six galaxies with aberrant emission (Section 2.5.2) were excluded from this analysis.

Indices omitted	N	Δlog(Age)	Δ[Fe/H]	Δ[E/Fe]	Δ[Z/H]	Early Type log(Age) vs [Fe/H]	Early Type log(Age) vs [E/Fe]	Late Type log(σ) vs [Fe/H]
WITH ENHANCEMENT								
None	20	0.000(0.000)	0.000(0.000)	0.000(0.000)	0.000(0.000)	0.089	0.041	0.087
$H\delta_F$,$H\gamma_F$	18	−0.020(0.026)	0.005(0.016)	0.008(0.021)	0.012(0.020)	0.089	0.037	0.077
$H\delta_{A,F}$,$H\gamma_{A,F}$	16	−0.030(0.044)	0.002(0.023)	0.013(0.020)	0.015(0.022)	0.084	0.031	0.073
$H\beta$	19	0.021(0.066)	−0.011(0.037)	−0.004(0.026)	−0.015(0.050)	0.087	0.050	0.098
$H\beta$,$H\delta_{A,F}$,$H\gamma_{A,F}$	15	−0.007(0.090)	−0.009(0.042)	0.006(0.027)	−0.003(0.056)	0.091	0.059	0.102
All except $H\beta$, Mg_2,⟨Fe⟩	3	−0.070(0.171)	0.004(0.129)	0.038(0.047)	0.040(0.156)	0.094	0.055	0.098
WITHOUT ENHANCEMENT								
None	20	−0.022(0.057)	–	–	0.035(0.028)	–	–	–
All except $H\beta$, [MgFe]	2	0.041(0.157)	–	–	0.039(0.128)	–	–	–

modest offsets. However, the scatter is large (∼0.15 dex). Scatter about the key correlations are also found to be increased in this case. These results emphasize the advantage of the large number of indices included in this study.

The effects on the results of ignoring enhancements are also shown in Table 11. To obtain this comparison, the best fits of our data (all 20 indices) to unenhanced SSP index values were found. It was assumed that $[Fe/H]_{SSP}$ of the best-fitting SSP best represents the value of [Z/H] for the population. Comparison of the values of log(Age) and [Z/H], estimated in this way, to the values given in Table 10 (derived by the Fe− method), show that the average difference between values are <0.05 dex in both parameters.

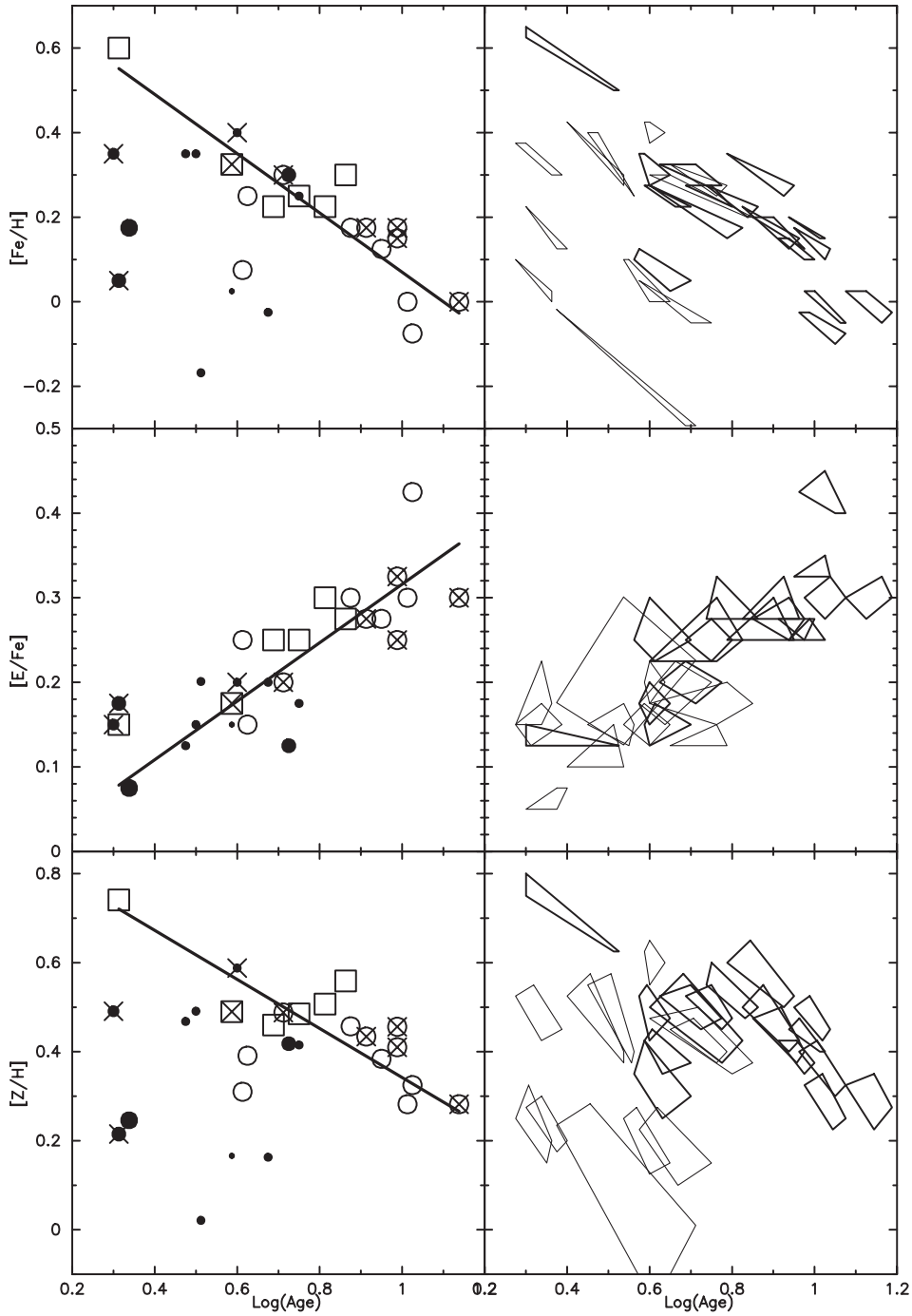

Figure 12. Luminosity-weighted [Fe/H], [E/Fe] and [Z/H] are plotted against log(Age). Recall that E represents the enhanced element group (Table 7, column 4). Data identified with an asterisk in Table 10 are omitted from this plot. Correlations for early-type galaxies are shown as lines. Key: ● = bulges, □ = S0, ○ = E, × = Virgo cluster galaxies. 1σ confidence contours from our fits are shown on the right.

Scatter about these differences are similarly $\lesssim 0.05$ dex. We also tested the method employed by some authors (e.g. Gonzalez 1993; Kuntschner & Davies 1998) of combining the Mgb and ⟨Fe⟩ indices by taking their geometric mean ($\sqrt{Mgb\langle Fe\rangle}$) to make a new index ([MgFe]). Age and metallicity estimates are then made using this index and an age-sensitive index, normally Hβ. Results of the comparison between log(Age) and [Z/H] values derived using this method, and those derived from the Fe− method, are also shown in Table 11. The average differences between the two sets of values is similar in magnitude to those found above for all 20 indices (without enhancement). However, the scatter in the differences is significantly greater (~ 0.15 dex). This result again emphasizes the benefit of including a large number of indices in the fitting procedure.

4.6 Results from blue indices

Values for luminosity-weighted log(Age), [Fe/H], [Z/H] and [E/Fe] derived by the Fe− method detailed above, are given in Table 10. Plots of [Fe/H], [Z/H] and [E/Fe] against log(Age) are shown in

Table 12. Correlations with log(Age). The number of galaxies fitted (N) and best-fitting slopes and intercepts (errors in brackets) are given. Also shown are the (unweighted) correlation coefficient (r) and χ^2 values.

	N	Slope	Intercept	r	χ^2
E/S0s					
Fe/H]	17	−0.701(0.167)	0.771(0.139)	−0.81	71
E/Fe]	17	0.346(0.116)	−0.030(0.099)	0.78	65
Z/H]	17	−0.551(0.243)	0.893(0.202)	−0.66	70
Bulges					
Fe/H]	11	1.658(1.604)	−0.582(0.814)	−0.01	93
E/Fe]	11	0.364(0.253)	−0.039(0.11)	0.34	45
Z/H]	11	1.538(1.410)	−0.387(0.702)	0.06	55

Table 13. Correlations with log(σ_0). The number of galaxies fitted (N) and best-fitting slopes and intercepts (errors in brackets) are given. Also shown are the (unweighted) correlation coefficient (r) and χ^2 values.

	N	Slope	Intercept	r	χ^2
E/S0s					
Log(Age)	17	1.655(0.690)	−3.079(1.642)	0.74	110
Fe/H]	17	−0.727(0.881)	1.906(2.089)	−0.55	159
E/Fe]	17	0.422(0.461)	−0.735(1.091)	0.39	117
Z/H]	17	−0.553(0.688)	1.736(1.631)	−0.53	31
Bulges					
Log(Age)	11	0.811(1.053)	−1.265(2.277)	0.54	38
Fe/H]	11	1.043(0.495)	−2.023(1.093)	0.80	49
E/Fe]	11	0.246(0.423)	−0.401(0.917)	0.04	25
Z/H]	11	1.177(0.338)	−2.169(0.750)	0.85	15

Fig. 12. To avoid confusion, points with errors >0.2 dex, or limits, (see Table 10) have been omitted from these plots. Confidence contours (1σ, allowing for three interesting parameters) are plotted on the right of Fig. 12 as quadrilaterals with vertices at extremes projected on to the plane presented. The alignment of the contours in plots of [Z/H] and [Fe/H] against log(Age) clearly show the age/metallicity degeneracy. However, the size of the contours suggests that, for the majority of galaxies, the degeneracy has been broken.

It can be seen in Fig. 12 that the ages of spiral bulges, S0s and Es form a continuous, overlapping sequence of increasing luminosity-weighted age, with bulges ranging from 1.5 to 6 Gyr old, while S0s and Es range from 2 to 7 Gyr and 4 to 13 Gyr respectively. S0s also appear more Fe− rich than Es. This is reflected in the strong central Fe features seen in S0s (e.g. Figs 4 and 6).

We fitted lines (by χ^2 minimization) to both the early- and late-type data plotted in Fig. 12. The four galaxies identified by asterisks in Table 10 were omitted from the fitting procedure. Table 12 give the results of our fits. These have been calculated as the average of the fits obtained when y-axis and x-axis deviations are minimized separately. Errors quoted in Table 12 are half the difference between the values from these two fits. Significant correlations are shown as lines in Fig. 12. We find a strong anticorrelation between [Fe/H] and luminosity-weighted log(Age) in early-type galaxies. However, it was a concern that this may be heavily influenced by the young S0 galaxy (NGC 2549). We therefore re-calculated the correlation omitting this galaxy. A slope of 0.672 ± 0.193 was found, indicating that this point is not having an excessive influence (cf. Table 12). We also detect a strong correlation between [E/Fe] and log(Age) in early-type galaxies. These trends are reflected in the index–index plots of Fig. 9 (Section 3.3.1). The anticorrelation between [Z/H] (calculated by equation 3) and log(Age) is a natural consequence of the somewhat

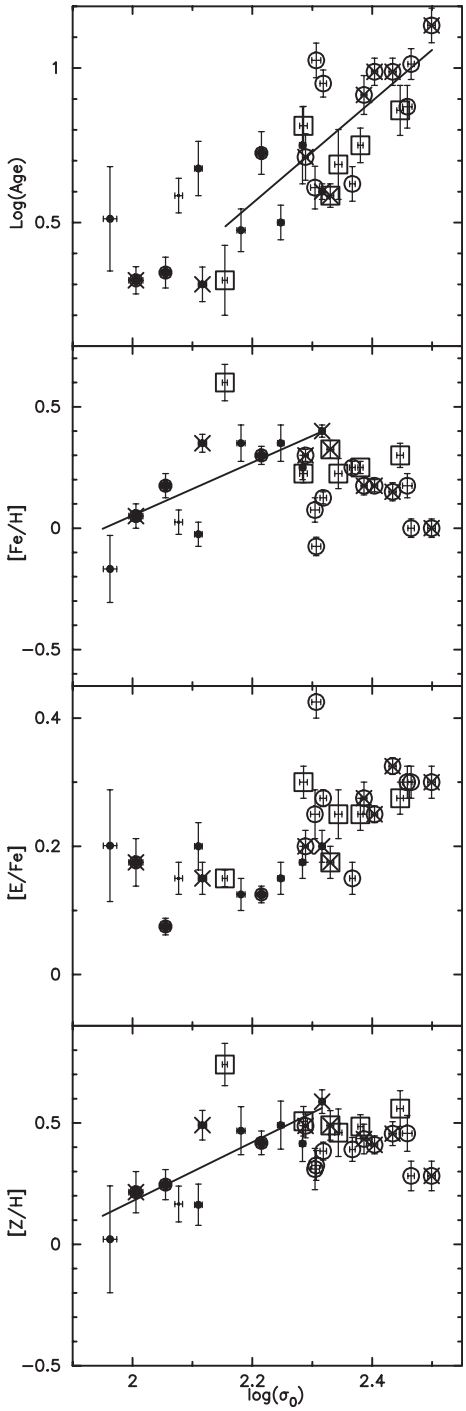

Figure 13. Luminosity-weighted log(Age), [Fe/H], [E/Fe] and [Z/H] are plotted against the log of central velocity dispersion. Symbols as in Fig. 12.

stronger correlations with [Fe/H] and [E/Fe]. Both the (relatively young) S0s and the five Virgo cluster, ellipticals (which are amongst the oldest in our sample) appear to follow the same trends as the early-type sample as a whole. We find that elliptical galaxies tend to be older and more metal-poor than S0 galaxies. No significant correlations were found in late-type galaxies. However, the [E/Fe] − log(Age) plot shows that the data for early and late types form a continuous monotonic locus. This correlation may then be common to both Hubble types.

Luminosity-weighted log(Age), [Fe/H], [Z/H] and [E/Fe] are

plotted against log of central velocity dispersion in Fig. 13. Fits to these data (minimizing χ^2) are given in Table 13. Values given are from fits with y-axis errors only (which dominate in most cases). However, errors given are half the difference between the quoted fit and the x-axis error only fit. Correlations with $\geq 3\sigma$ significance are shown as lines in Fig. 13. There is a trend for luminosity-weighted age to increase with central velocity dispersion in our early-type galaxy sample. This trend is also consistent with the late-type data. However, we find no significance in the correlation of age versus velocity dispersion in late types (Table 13). The trend of increasing [E/Fe] with velocity dispersion for early-type galaxies suggested by Fig. 13 also has very low significance, particularly when compared to the strength of the correlation of [E/Fe] with log(Age) in early-types. Our data therefore suggest that, in the early-type galaxies in our sample, the stronger correlations of both [E/Fe] and velocity dispersion with log(Age) are the cause of the apparent trend of [E/Fe] with velocity dispersion. Bulges, on the other hand, while showing no significant correlations with age, show strong correlations of [Fe/H] and [Z/H] with velocity dispersion and only marginal (approximately constant) enhancement with respect to solar, i.e., [E/Fe] $\sim +0.15$. Thus our results suggest that while the principal parameter controlling abundances and abundance ratios in early-type galaxies is age, in bulges it is central velocity dispersion.

We have compared the trends in our early-type galaxy sample with the results of Trager et al. (2000b) and Kuntschner et al. (2001). Both authors find an anticorrelation between age and metallicity that is approximately aligned with the age/metallicity degeneracy. These correlations are in good agreement with the anticorrelation found in our early-type sample (Fig. 12). Trager et al. (2000b) also found an offset of the age-metallicity relation with lower velocity dispersion. Future spectral observations of low velocity dispersion ellipticals with high signal-to-noise ratios are needed to further investigate these trends, incorporating large numbers of indices.

4.7 Results from red indices

Estimation of age and metallicity from the NIR data is difficult, as the only age-sensitive indices are in the blue wavelength range. We must therefore combine indices from populations that may differ, e.g., Hβ versus CaT in Fig. 10. The NIR indices were also not modelled by TB95, so abundance ratio effects can not be estimated. We have none the less derived log(Age) and [Fe/H] estimates from the calcium triplet indices and Hβ. The Mg I index was excluded as, contrary to expectation, the positions of values of this index with respect to the SSP grids imply *lower* metallicities than do values of the CaT index. Many of the early-type galaxy data points also imply ages greater than 17 Gyr. We therefore assume that this index is affected by some, as yet unidentified, calibration error (either in our reductions or in the SSP estimates). Values of log(Age) derived from the calcium triplet and Hβ index are higher than those given in Table 10 by ~ 0.15, while [Fe/H] estimates are lower by ~ 0.2 dex. While we observe that these estimates are, qualitatively, in line with our results from blue indices, we make no further attempt at interpretation of these NIR data.

5 COMPARISON WITH COMPOSITE MODELS

In this section we generate models with composite SFHs, and compare the predictions with our observations in an effort to understand galaxy histories. The composite model code was first described in Sansom & Proctor (1998), where we assumed solar abundance ratios. Here we extend the models to incorporate non-solar abundance ratios. 14 elements (listed in Table 7) are followed self-consistently. These cover most of the heavy-element mass loss from SNII, SNIa and intermediate mass stars. Our models can allow for inflow of gas (enriched to the current level of the ISM or of primordial composition) into a single zone. The lowest metallicity modelled by W94 is for $Z = Z_{\odot}/100$. Therefore we start the models with $10^6\,M_{\odot}$ of gas containing this small amount of metals ($Z = 2 \times 10^{-4}$ by mass fraction), assuming solar abundance ratios within this initial metallicity. Low-metallicity stars in our Galaxy have an increasing excess of α-element abundances (as described by equation 5). We allow for this in the composite models via the denominator in the exponent of equation (7), which is varied by up to a factor of 3 for α-elements in the SSP stars. Allowance for α-enhanced SSPs at low metallicity did not produce large effects in the predicted line-strengths in galaxies, which are dominated by higher metallicity stars. We use V99 SSPs and the T00a method to allow for non-solar abundance ratios in the composite models, calling on predictions of line-strength changes modelled by TB95. The rate of SNIa is a parameter in our models. In the current models we use a rate of 3.8×10^{-5} SNIa $\mathrm{Gyr}^{-1}\mathrm{M}_{\odot}^{-1}$. This is approximately that inferred in our Galaxy (Timmes, Woosley & Weaver 1995), which has an uncertainty of about a factor of 2. Larger SNIa rates will produce stronger iron-sensitive lines. We assume a Schmidt law with an index of one for the star formation rate (SFR $= C \times$ gas density), and a Salpeter initial mass function (IMF).

5.1 Primordial collapse

For the primordial model we started with $C = 4.0\,\mathrm{Gyr}^{-1}$, and a rapid, enriched inflow rate of $10^7\,\mathrm{M}_{\odot}\,\mathrm{Gyr}^{-1}$, going down to a more steady rate of $C = 0.2\,\mathrm{Gyr}^{-1}$ and zero inflow after 0.4 Gyr. Star formation is followed up to 1.5 Gyr ago. In a previous paper (Proctor et al. 2000) we showed that (assuming solar abundance ratios) rapid collapse and star formation in a primordial gas cloud does not produce strong enough metal absorption lines when compared with observations of early-type galaxies and spiral bulges. We confirm this result here with our non-solar ratio models. This is shown in Figs 8 and 9, where the thickest, short line indicates our predictions for such a primordial collapse model, for times ranging from 10 to 17 Gyr after the start of star formation. These primordial models include a higher rate of 7.6×10^{-5} SNIa $\mathrm{Gyr}^{-1}\mathrm{M}_{\odot}^{-1}$. The predicted metal line-strengths are too low to account for the observed line-strengths. Thus the conventional picture of spheroid formation through rapid, early collapse, followed by passive evolution, is ruled out by the observed strong lines. A similar conclusion was found for nearby spheroids by Worthey, Dorman & Jones (1996) and is analogous to the well-known G-dwarf problem in our own Galaxy, where there are insufficient low-metallicity stars compared to predictions of closed-box models with stars generated with a Salpeter IMF.

5.2 Models with extended inflow

In Proctor et al. (2000) we found that observations of spiral bulges could be explained with extended inflow models, with gas inflow over several Gyr enriched to the current level of the ISM. This assumed solar abundance ratios. Allowing for non-solar ratios, we find that such models tend to underproduce Fe− sensitive features. This is because the early feedback from SNII is extremely Mg-rich

compared to Fe (several 10s of times solar ratios – see the SNII models of Woosley & Weaver 1995). To produce models which can simultaneously explain Fe− and Mg-sensitive spectral features, a delayed burst of star formation seems to be needed to allow the ISM to first become enriched with Fe peak products from SNIa. Such models are preliminarily explored in the next section.

5.3 Merger models

With a delayed burst of star formation we begin to be able to produce models which can simultaneously explain the strengths of several spectral features. A full exploration of SFH parameter space is beyond the scope of this paper and will be the subject of future work. However, in Figs 8 and 9 we illustrate predictions of line-strengths for merger models with an associated burst of star formation several Gyr after the start of the SFH (delayed burst models – medium thick short line). Present-day predictions (at 17 Gyr) for models with a burst ranging from 3 to 13 Gyr delay are shown. The parameters used to describe the composite merger model shown here are $C = 4.0\,\mathrm{Gyr}^{-1}$ initially, with low, enriched inflow rate of $1 \times 10^4\,\mathrm{M}_\odot\,\mathrm{Gyr}^{-1}$, increasing to $10^7\,\mathrm{M}_\odot\,\mathrm{Gyr}^{-1}$ during the starburst. This rapid starburst lasts for 0.4 Gyr, after which the inflow is set to zero, so the remaining gas is rapidly used up in star formation. We see that these examples reach the regions populated by early-type galaxies, for most Fe− and Mg-sensitive line-strengths. An exception is Fe5406 (but see Fig. 4 and Section 3.2.1). Interestingly, we find that the models tend to underpredict carbon-sensitive features (⟨CN⟩, $C_2$4668). This may indicate that all the sources of carbon enrichment have not been accounted for in our models. Indeed, carbon enhancements in some very low-metallicity stars in our own Galaxy are hard to explain (Norris, Ryan & Beers 1997), and dredge-up models for the contributions of carbon from intermediate-mass stars are uncertain. Stars produced in the delayed burst have lower overall [E/Fe] than the earlier star formation, since SNIa have had time to accumulate Fe in the ISM. Thus these model predictions tend to support the idea of ellipticals forming by mergers of galaxies, with enriched gas inflow and enhanced star formation during the merger.

There are few predictions of detailed galaxy properties from hierarchical merger models. However, Kauffmann (1996) used a semi-analytic model of galaxy formation in both field and cluster environments to make testable predictions for the ages of various Hubble types in differing environments. In these models early-type galaxies form by the merger of two, roughly equal-mass, progenitor galaxies, while spiral galaxies form by accretion of a disc on to a pre-formed elliptical galaxy. Kauffmann found luminosity-weighted ages for early types between 5 and 12.5 Gyr, in good agreement with our findings. Kauffmann also found cluster ellipticals to be ∼4 Gyr older than ellipticals in low-density environments. This is again consistent with our findings, as the five Virgo cluster ellipticals are amongst the oldest in our sample. The positive correlation between age and velocity dispersion in elliptical galaxies is qualitatively consistent with the relationship proposed by Forbes & Ponman (1999) for σ versus merger redshift. Consequently, while both primordial collapse and extended inflow models fail to reproduce the main features of our data without recourse to additional physics (a biased IMF or Population III stars), the hierarchical model of early-type galaxy formation by merger agrees well.

For the bulges of spirals, Kauffmann (1996) predicts ages significantly lower than those in ellipticals, in agreement with our findings. However, Kauffmann also predicts a correlation between bulge ages and the luminosity of their discs. Inspecting the distribution of Hubble types (indicated by solid symbol sizes in Figs 12 and 13), we find no evidence of a trend in age with spiral Hubble type. Therefore this prediction is at odds with our findings. Kauffmann does point out, however, that the correlation may be hidden if there is significant inflow of gas from the disc, perhaps due to the formation of bars. Many of the bulges in our sample show strong evidence for kinematic substructure and on-going star formation (i.e., emission). Our bulges also possess [Mg/Fe] values too low to have been formed in a single primordial burst (see Fig. 8). These observations, and the absence of a correlation between age and Hubble type, support the idea that disc inflow must play an important role in the star formation histories in bulges.

6 CONCLUSIONS

We have derived luminosity-weighted log(Age), iron abundance, abundance ratios and metallicity (log(Age), [Fe/H], [E/Fe] and [Z/H] respectively) in the centres of 32 galaxies, ranging in Hubble type from E to Sbc. We used 20 indices for which V99 modelled SSPs, plus their sensitivities to individual elements as tabulated in TB95, to model the effects of non-solar abundance ratios in these galaxies. We find that ignoring such enhancements leads to reasonably accurate age and metallicity estimates, but that using many fewer indices (e.g., three) leads to larger errors in derived values (see Table 11). By using many indices and modelling abundance ratios, we are able to probe correlations between derived parameters much more accurately.

Our sample of early-type galaxies spans a wide range of ages (2 to 13 Gyr) with the five Virgo cluster ellipticals amongst the oldest. These E/S0 galaxies show correlations of both velocity dispersion (σ) and [E/Fe] with age, while [Fe/H] and [Z/H] both show anticorrelations with age. [Fe/H], [Z/H] and [E/Fe] show no significant correlation with σ over the small range in σ covered by our E/S0 galaxies. These results are at odds with the predictions of primordial collapse models, which predict uniformly old, early-type galaxies and increasing [Z/H] with σ. However, the correlations suggest that the main parameter controlling the metal content of our bright, early-type galaxies is age. Our results are consistent with the predictions of hierarchical merger models of galaxy formation (e.g. Kauffmann 1996) which predict the observed E, S0 (and bulge) age sequence. The observed correlation between age and velocity dispersion is in qualitative agreement with the relationship proposed by Forbes & Ponman (1999) for merger remnants. The strong correlation of [E/Fe] with log(Age) and anticorrelation of [Fe/H] with log(Age) are qualitatively reproduced by our merger models of galaxy formation (Section 5.3 and Fig. 9). In our models these trends are the result of the shortening interval (in which SNIa can produce Fe) between the commencement of star formation and the final merger event. Thus we find several observational results that agree with the predictions of merger models for early-type galaxies.

The correlations outlined above in turn call for careful interpretation of Lick index versus σ correlations. For instance, high Mg_2, high velocity dispersion, early-type galaxies are amongst the most metal-*poor* in our sample. Any correlation of Mg_2 with σ, may in fact, reflect an increasing age and *enhancement* ([E/Fe]) with velocity dispersion (indicating mass) not, as is usually assumed, a metallicity–mass relation (see also related comments in the conclusion of Trager et al. 2000b).

The anticorrelations of [Fe/H] and of [Z/H] with log(Age) could also have implications for the interpretation of colour–magnitude

diagrams of these objects. This can be illustrated by the extremely narrow range of optical colours [$\Delta(U-V) \sim 0.08$ for SSPs ranging in age from 3 to 17 Gyr) predicted for SSPs that follow the age–[Fe/H] anticorrelation shown by our early-type galaxy sample. Colour–magnitude correlations have also been interpreted as metallicity–mass relations on the basis of monolithic collapse models for the formation of elliptical galaxies (e.g. Kodama et al. 1998). Our results from line-strengths suggest that merger models must be considered before this interpretation of the observed correlations can be relied on.

We detect significant differences between early-type galaxies and spiral bulges. Es, S0s and bulges in our sample form a continuous overlapping sequence of decreasing luminosity-weighted age, with bulges typically 2 Gyr younger than S0s, and 5 Gyr younger than Es. This is again in line with the predictions of Kauffmann (1996), for galaxies in low-density environments. We find no significant correlations with age in bulges. However, correlations of [Fe/H] and [Z/H] with σ are strong. Thus the main parameter controlling the metal content of bulges is σ. Kauffmann predicts a correlation between bulge-to-disc ratio and age in spiral galaxies. We detect no such correlation in our data. However, Kauffmann also points out that if significant inflow from the disc occurs, after a merger, this correlation may be lost. The relatively low values of [E/Fe] ($\sim +0.15$) in bulges and the strong correlations of metals with σ are consistent with such a model of bulge formation. The correlations of [Fe/H] and [Z/H] with σ in spiral bulges means that we interpret the correlations of Lick indices with σ found in this work (Figs 4 and 5 and Table 5) as a metallicity–mass relation, in contrast to our finding for early-type galaxies.

In conclusion, we have shown that primordial collapse models of galaxy formation are unable to reproduce the line-strengths observed in the spheroids of galaxies, while merger models can. Derived ages and correlations between derived parameters differ significantly between early- and late-type galaxies, suggesting that, at least at some point in their evolution, the star formation histories in these objects must have differed significantly. We therefore contend that the similarities in morphology and photometric properties in these objects, noted in the introduction, are the result of the various degeneracies at work rather than indicating similar formation processes.

ACKNOWLEDGMENTS

The authors acknowledge the data analysis facilities provided by the Starlink Project, which is run by CCLRC on behalf of PPARC. In addition, the IRAF software package was used. IRAF is distributed by the National Optical Astronomy Observatories, which is operated by AURA, Inc., under cooperative agreement with the National Science Foundation. This work is based on observations made with the William Herschel Telescope, operated on the island of La Palma, by the Isaac Newton Group in the Spanish Observatorio del Instituto de Astrofisica, Roque de los Muchachos de Canarias. Travel funds were provided by PPARC and the University of Central Lancashire. Thanks are due to our colleagues G. Bromage and C. Haines for comments on this paper prior to submission, and also to the referee, Scott Trager, for careful reading and improvement of this paper.

REFERENCES

Balcells M., Peletier R. F., 1994, AJ, 107, 135
Barnes J. E., Hernquist L., 1996, ApJ, 471, 115
Bender R., Burstein D., Faber S. M., 1993, ApJ, 411, 153
Bender R., Saglia R. P., Ziegler B., Belloni P., Greggio L., Hopp U., Bruzual G., 1998, ApJ, 493, 529
Bernardi M., Renzini A., da Costa L. N., Wegner G., Alonso M. V., Pellegrini P. S., Rité C., Willmer C. N. A., 1998, ApJ, 508, L143
Bertelli G., Bressan A., Chiosi C., Fagotto F., Nasi E., 1994, A&AS, 106, 275
Carlberg R. G., 1984, ApJ, 286, 403
Ciotti L., D'Ercole A., Pellegrini S., Renzini A., 1991, ApJ, 376, 380
Concannon K. D., Rose J. A., Caldwell N., 2000, ApJ, 536, L19
Cox A. N., 2000, Allen's Astrophysical Quantities, 4th ed. AIP Press, Springer-Verlag, New York, p. 29
Davies R. L., Sadler E. M., Peletier R. F., 1993, MNRAS, 262, 650
de Vaucouleurs G., de Vaucouleurs A., Corwin H. G., Buta R. J., Paturel G., Fouqué P., 1991, Third Reference Catalogue of Bright Galaxies. Springer-Verlag, New York (RC3)
Diaz A. I., Terlevich E., Terlevich R., 1989, MNRAS, 239, 325
Edvardsson B., Andersen J., Gustafsson B., Lambert D. L., Nissen P. E., Tomkin J., 1993, A&A, 275, 101
Faber S. M., 1973, ApJ, 179, 731
Faber S. M., Friel E. D., Burstein D., Gaskell C. M., 1985, ApJS, 57, 711
Feltzing S., Gustafsson B., 1998, A&AS, 129, 237
Fisher D., Franx M., Illingworth G., 1996, ApJ, 459, 110
Forbes D. A., Ponman T. J., 1999, MNRAS, 309, 623
González J. J., 1993, PhD thesis, Univ. California
Gorgas J., Faber S. M., Burstein D., González J. J., Courteau S., Prosser C., 1993, ApJS, 86, 153
Gorgas J., Pedraz S., Guzmán R., Cardiel N., González J. J., 1997, ApJ, 481, L19
Goudfrooij P., Emsellem E., 1996, A&A, 306, L45
Goudfrooij P., Gorgas J., Jablonka P., 1999, Ap&SS, 269, 109
Greggio L., 1997, MNRAS, 285, 151
Gustafsson B., Kjærgaard P., Andersen S., 1974, A&A, 34, 99
Hansen L., Kjærgaard P., 1971, A&A, 15, 123
Henry R. B. C., Worthey G., 1999, PASP, 111, 919
Idiart T., Thévenin F., 2000, ApJ, 541, 2071
Idiart T., de Freitas Pacheco J. A., Costa R. D. D., 1996, AJ, 112, 2541
Jablonka P., Martin P., Aromoto N., 1996, AJ, 112, 1415
Jørgensen I., 1997, MNRAS, 288, 161
Jørgensen I., 1999, MNRAS, 306, 607
Kauffmann G., 1996, MNRAS, 281, 487
Kauffmann G., White S. D. M., Guiderdoni B., 1993, MNRAS, 264, 201
Khosroshahi H. G., Wadadekar Y., Kembhavi A., 2000, ApJ, 533, 162
Kodama T., Arimoto N., Barger A. J., Aragón-Salamanca A., 1998, A&A, 334, 99
Kuntschner H., 2000, MNRAS, 315, 184 (K00)
Kuntschner H., Davies R. L., 1998, MNRAS, 295, L29
Kuntschner H., Lucey J. R., Smith R. J., Hudson M. J., Davies R. L., 2001, MNRAS, 323, 615
Lebreton Y., Perrin M.-N., Cayrel R., Baglin A., Fernandes J., 1999, A&A, 350, 587
Norris J. E., Ryan S. G., Beers T. C., 1997, ApJ, 488, 350
O'Connell R. W., 1976, ApJ, 206, 370
Osterbrock D. E., 1989, Astrophysics of Gaseous Nebulae and Active Galactic Nuclei. University Science Books, Mill Valley
Proctor R. N., Sansom A. E., Reid I. N., 2000, MNRAS, 311, 37
Prugniel P., Simien F., 1997, Web site, ftp://ftp-obs.univ-lyon1.fr/pub/galaxies/data/kinematics/sigma97.txt
Ryan S. G., Norris J. E., Bessell M. S., 1991, AJ, 102, 303
Salaris M., Weiss A., 1998, A&A, 335, 943
Salasnich B., Girardi L., Weiss A., Chiosi C., 2000, A&A, 361, 1023
Sansom A. E., Proctor R. N., 1998, MNRAS, 297, 953
Tantalo R., Chiosi C., Bressan A., 1998, A&A, 333, 419
Timmes F. X., Woosley S. E., Weaver T. A., 1995, ApJS, 98, 617
Trager S. C., 1998, PhD thesis, Univ. California
Trager S. C., Worthey G., Faber S. M., Burstein D., González J. J., 1998, ApJS, 116, 1

Trager S. C., Faber S. M., Worthey G., González J. J., 2000a, AJ, 119, 1645 (T00a)
Trager S. C., Faber S. M., Worthey G., González J. J., 2000b, AJ, 120, 165
Tripicco M. J., Bell R. A., 1995, AJ, 110, 3035 (TB95)
Tully R. B., 1988, Nearby Galaxies Catalogue. Cambridge Univ. Press, Cambridge
Vanden Berg D. A., Swenson F. J., Rogers F. J., Iglesias C. A., Alexander D. R., 2000, ApJ, 532, 430
Vazdekis A., 1999a, ApJ, 513, 224 (V99)
Vazdekis A., 1999b, http://www.iac.es/galeria/vazdekis/col_lick.html (V99)
Vazdekis A., Casuso E., Peletier R. F., Beckman J. E., 1996, ApJS, 106, 307 (V96)
Vazdekis A., Peletier R. F., Beckman J. E., Casuso E., 1997, ApJS, 111, 203
Woosley S. E., Weaver T. A., 1995, ApJS, 101, 181
Worthey G., 1994, ApJS, 95, 107 (W94)
Worthey G., 1998, PASP, 110, 888
Worthey G., Ottaviani D. L., 1997, ApJS, 111, 377
Worthey G., Faber S. M., González J. J., 1992, ApJ, 398, 69
Worthey G., Faber S. M., González J. J., Burstein D., 1994, ApJS, 94, 687
Worthey G., Dorman B., Jones L. A., 1996, AJ, 112, 948

APPENDIX A: VELOCITY DISPERSION CORRECTIONS

A1 Characterization of stellar indices with spectral broadening

For accurate calibration, indices in galaxy spectra require correction to account for the effects of internal stellar velocity dispersion. Consequently, the indices of a subsample of Lick calibration stars were measured after convolving their spectra with Gaussians of a range of widths. 15 stars (spectral types G8 to K3), which best matched the spectral energy distributions of the galaxies, were used for the blue indices. In the red, all 24 Lick calibration stars were found to match galaxy spectra well. For each index a correction factor was calculated at each value of broadening. For most line indices, the correction factor was calculated as the ratio (C_i) of the index value at the Lick resolution to that at each value of broadening, i.e:

$$C_i = I_{\rm L}/I_{\rm Meas}, \tag{A1}$$

where $I_{\rm L}$ is the index value at the calibration resolution, and $I_{\rm Meas}$ is the index value in the broadened spectrum.

For molecular band indices (CN1, CN2, Mg_1 and Mg_2) and indices with ranges spanning zero (Hδ and Hγ indices), correction factors were calculated as the *difference* between the measured index and that at the calibration resolution at each value of broadening, i.e.,

$$C_i = I_{\rm L} - I_{\rm Meas}. \tag{A2}$$

The appropriate correction factor was calculated for each index, at each value of broadening, by averaging values from the stellar subsamples. A polynomial fit of order 3 was found such that

$$C_i = x_0 + x_1\sigma_C + x_2\sigma_C^2 + x_3\sigma_C^3, \tag{A3}$$

where σ_C is the width of the Gaussian (in km s^{-1}) convolved with the stellar spectrum at $\sigma_{\rm L}$. Behaviours of the indices of the stellar sample with broadening above the Lick resolution are shown in Fig. A1 as lines. These are in good agreement with the behaviours of indices measured by previous authors (e.g. Kuntschner 2000). The nature of the applied velocity dispersion corrections, i.e., whether C_i should be multiplied by the raw index value or added to the raw value are indicated in the plots and summarized in column 2 of Table A1. This table also gives a typical uncertainty in the correction factor for each index, estimated as the rms scatter in the stellar values about the mean C_i at $\sigma_C = 200\,{\rm km\,s^{-1}}$. This corresponds to the appropriate value for a high velocity dispersion elliptical galaxy. When correction factors are used the scatter in the stellar data at the value of broadening appropriate to the galaxy was included in the statistical errors.

A2 Application to galaxies

To gain confidence in these polynomials, galaxy spectra were also broadened by convolution with Gaussians of a range of widths. The behaviour of the galaxies was then compared to that of the stellar subsample (Fig. A1). For most indices the galaxy data lie within the scatter of the stellar data. However, for a few indices, large scatter and/or small systematic differences in the behaviour of galaxies compared to the stellar data were observed. These indices (most noticeably Hδ, Ca4227 and Ca4455) are among those affected by the poor removal of the dichroic response. The scatter in the stellar data has been allowed for in our errors as described in Section 2.4.2. However, to test the possible impact of differences in behaviour between our samples of stars and galaxies, two velocity dispersion correction techniques were tested.

Technique 1

The first technique (which is generally used by other authors) is to broaden all galaxy spectra by a Gaussian of a width $\sigma_{\rm B}$, given by equation (1), prior to the measurement of indices. The resultant spectrum of a galaxy with velocity dispersion σ_V then has a total broadening (σ_G) given by

$$\sigma_G^2 = \sigma_{\rm I}^2 + \sigma_V^2 + \sigma_{\rm B}^2 \tag{A4}$$

$$= \sigma_{\rm L}^2 + \sigma_V^2. \tag{A5}$$

As the correction factors are dependent on the *excess* broadening of the galaxy with respect to $\sigma_{\rm L}$, the value $\sigma_C = \sigma_V$ is entered into the polynomials in Table A1 to obtain the correction factor C_i.

Technique 2

In the second technique, if the total broadening of the galaxy $(\sigma_{\rm I}^2 + \sigma_V^2)^{1/2}$ is less than the target calibration resolution ($\sigma_{\rm L}$), the galaxy spectrum is broadened up to the Lick resolution by convolution with a Gaussian of width $\sigma_{\rm B}$ given by

$$\sigma_{\rm B}^2 = \sigma_{\rm L}^2 - \sigma_{\rm I}^2 - \sigma_V^2. \tag{A6}$$

Consequently, as the spectrum has been broadened to the calibration resolution, the final index values can be measured directly from the broadened galaxy spectrum with no need for correction.

If, on the other hand, the total galaxy broadening is greater than $\sigma_{\rm L}$, then the spectra are left unbroadened, and $\sigma_C = (\sigma_{\rm I}^2 + \sigma_V^2 - \sigma_{\rm L}^2)^{1/2}$ is substituted into the polynomials to calculate the appropriate value of C_i.

It should be noted that for some indices (e.g., Hδ) the second technique involves no use of the polynomials, as all galaxies in our sample have $\sigma_{\rm L}^2 > \sigma_{\rm I}^2 + \sigma_V^2$. The two techniques agree well over our whole velocity dispersion range. This is true for all indices measured. Comparisons of the results from the two techniques can be found in Proctor (PhD thesis, in preparation). In this paper the second technique is used since it involves smaller corrections, thus minimizing the effects of systematic differences in the behaviour of the stellar and galaxy spectra with broadening.

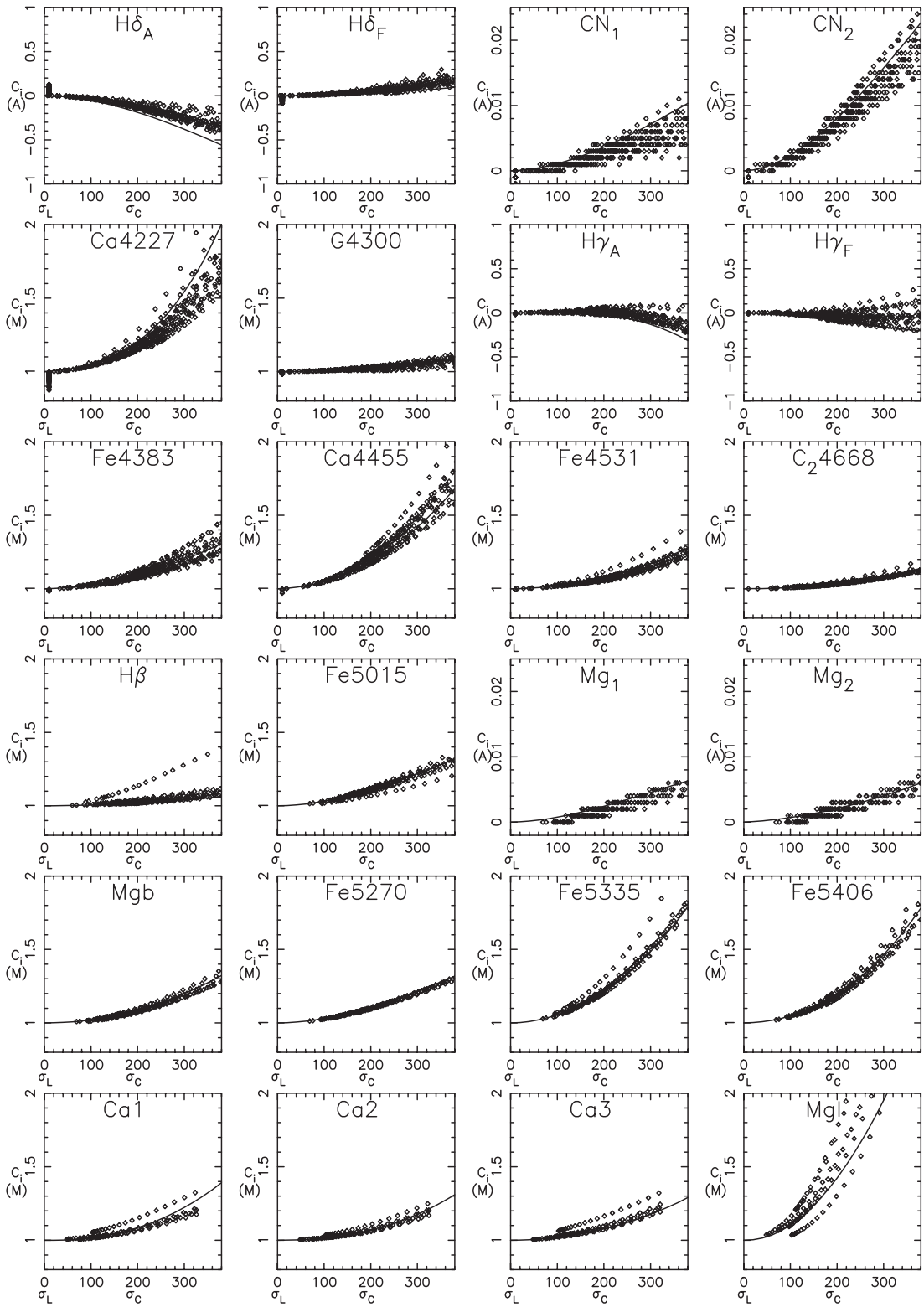

Figure A1. Behaviour of indices with broadening. Stellar correlations are shown as lines. Galaxy data are shown as points. Only galaxies with total observed broadening below σ_L are plotted.

Table A1. Polynomial coefficients relating the velocity dispersion correction factor (C_i; see text) to the correction velocity (σ_C).

Index	(A)dditive or (M)ultiplicative	Polynomial Coefficients (C_i versus σ_C in km s^{-1}) x_0	x_1 ($\times 10^{-3}$)	x_2 ($\times 10^{-6}$)	x_3 ($\times 10^{-9}$)	Uncertainty in correction at $\sigma_C = 200$ km s^{-1}
Hδ_A	A	0.0	−0.058	−5.195	3.894	0.029 Å
Hδ_F	A	0.0	−0.005	0.704	−0.077	0.019 Å
CN$_1$	A	0.0	0.002	0.097	−0.081	0.001 mag
CN$_2$	A	0.0	0.003	0.225	−0.201	0.001 mag
Ca4227	M	1.0	0.231	1.246	13.400	3.3 per cent
G4300	M	1.0	0.021	0.480	0.133	0.4 per cent
Hγ_A	A	0.0	0.006	1.181	−8.883	0.053 Å
Hγ_F	A	0.0	−0.079	−2.751	4.096	0.054 Å
Fe4383	M	1.0	0.037	2.334	−0.811	1.7 per cent
Ca4455	M	1.0	0.086	3.941	1.424	4.1 per cent
Fe4531	M	1.0	0.033	1.608	0.628	1.4 per cent
C$_2$4668	M	1.0	−0.001	0.851	0.284	0.5 per cent
Hβ	M	1.0	0.031	0.213	0.384	1.0 per cent
Fe5015	M	1.0	0.040	3.025	−2.443	1.1 per cent
Mg$_1$	A	0.0	0.002	0.067	−0.073	0.001 mag
Mg$_2$	A	0.0	0.004	0.035	−0.008	0.001 mag
Mgb	M	1.0	−0.003	2.129	0.307	0.4 per cent
Fe5270	M	1.0	0.024	3.027	−2.352	0.5 per cent
Fe5335	M	1.0	0.059	4.748	1.522	0.6 per cent
Fe5406	M	1.0	0.050	3.927	3.565	1.2 per cent
Ca1	M	1.0	−0.053	1.892	2.526	0.1 per cent
Ca2	M	1.0	0.004	1.248	2.339	0.1 per cent
Ca3	M	1.0	0.028	1.592	0.909	0.1 per cent
Mg I	M	1.0	−0.082	11.286	−1.443	0.1 per cent

This paper has been typeset from a TEX/LATEX file prepared by the author.